Università degli Studi di Padova

Dipartimento di Fisica e Astronomia "Galileo Galilei"
Corso di Laurea Magistrale in Fisica

Phase I of the ANNIE experiment: Data Acquisition system and preliminary data analysis

Relatore
Dott. Gianmaria Collazuol

Correlatori:
Prof. Francesca Di Lodovico (QMUL)
Dr. Benjamin Richards (QMUL)

Candidato:
Tommaso Boschi
matr. 1105506

Anno Accademico 2015/2016

Agli amici più grandi.
A chi ho perso per strada.

Overview

My thesis work is placed in the context of the the Accelerator Neutrino Neutron Interaction Experiment (ANNIE), a water Cherenkov detector built at the Fermi National Accelerator Laboratory (FNAL). The main aim of ANNIE is to study in depth the nature of neutrino-nucleus interactions by analysing the yield of final state neutrons. New technologies, such as gadolinium-loaded water and, for the first time, Large Area Picosecond Photodetectors (LAPPDs) will be also employed in future phases of the experiment. The measurement will have relevant implications for the next generation water Cherenkov detectors, in which these techniques may play a significant role in reducing backgrounds to the proton decay measurements, supernova neutrino observations and neutrino interaction physics.

The thesis deals with the phase I of the experiment, in which conventional photomultipliers (PMTs) are adopted within the tank, and the forward veto and the Muon Range Detector (MRD) are partially being employed. A small container, called neutron volume capture (NVC) is also located inside the tank, for preliminary neutron yield studies. The main work consists in the development of the CAMAC electronics Data Acquisition system (DAQ); the already existing VME electronics DAQ, for the water PMTs, is also described. Early stage data are analysed, and original event reconstruction techniques are proposed.

The R&D activities were conducted within the Particle Physics Research Group (PPRC) of the Queen Mary University of London.

In Chapter 1, Neutrino physics is briefly introduced, with a particular interest on the interactions with nucleons and experimental techniques for their detection. The concept and the apparatus of ANNIE experiment is described in Chapter 2, while the DAQ system is illustrated in Chapter 3. The data analysis topic is split in two chapters. The algorithm developed for signal discrimination from background is explained in Chapter 4, and the results of its application on preliminary data sets are shown in Chapter 5. Chapter 6 reports final considerations on the whole work, in view of the future stages of the experiment.

Contents

Chapter 1

Introduction

The Standard Model (SM) is a gauge theory that describes the strong, electromagnetic, and weak interactions of elementary particles in the framework of quantum field theory. The model is based on the local symmetry group

$$\mathrm{SU}(3)_C \otimes \mathrm{SU}(2)_L \otimes \mathrm{U}(1)_Y \tag{1.1}$$

where C, L and Y denote colour, left-handed chirality and weak hypercharge, respectively. The gauge group uniquely determines the interactions and the number of vector gauge bosons that correspond to the generators of the group. There are eight massless gluons that mediate strong interactions, corresponding to the eight generators of $\mathrm{SU}(3)_C$, and four gauge bosons, of which three are massive ($W^{\pm}$ and Z) and one is massless, corresponding to the three generators of $\mathrm{SU}(2)_L$ and one generator of $\mathrm{U}(1)_Y$, responsible for electroweak interactions. The symmetry group of the SM fixes the interactions, i.e. the number and properties of the vector gauge bosons, with only three independent unknown parameters: the three coupling constants of the $\mathrm{SU}(3)_C$, $\mathrm{SU}(2)_L$, and $\mathrm{U}(1)_Y$ groups, all of which must be determined from experiments. The number and properties of scalar bosons and fermions are left unconstrained, except for the fact that they must transform according to the representations of the symmetry group, while the fermion representations must lead to the cancellation of quantum anomalies. The known elementary fermions are divided in two categories, quarks and leptons, according to the following scheme:

Generation	**1st**	**2nd**	**3rd**
Quark	u	c	t
	d	s	b
Letpons	e	μ	τ
	ν_e	ν_μ	ν_τ

and their respective antiparticles. They are distinguished by the fact that quarks participate in all the interactions whereas leptons participate only in the electroweak interactions [1].

Electroweak interactions can be studied separately from strong interactions, because the symmetry under the colour group is unbroken and there is no mixing between the $\mathrm{SU}(3)_C$ and the $\mathrm{SU}(2)_L \otimes \mathrm{U}(1)_Y$ sectors. On the other hand, the Glashow, Salam, and Weinberg theory [2] well explains the group mixing between electromagnetic and weak interactions caused by a symmetry breaking process. This theory and the discovery of the predicted W and Z bosons, in addition to the gluon, the top, and charm quarks,

made the fortune of the Standard Model. Their predicted properties were experimentally confirmed with good precision and the recent discovery of the Higgs Boson [3] [4] is the latest crowning achievement of SM.

Despite being the most successful model of particle physics to date, the SM is actually limited in its approximation to reality, in that some clear evidences cannot be explained. The most outstanding breakthrough is the neutrino oscillations, which was awarded the Nobel Prize in Physics in 2015 [5] and has proved that the neutrinos are not all massless, as it is assumed by theory. Mass terms for the neutrinos can be included in the SM, with the implications of theoretical problems. Likewise, the SM is unable to provide an explanation of the observed asymmetry between matter and anti-matter. It was noted by Sakharov [6] that a solution to this puzzle would require some form of C and CP violation in the early Universe, along with Baryon number violation and out-of-equilibrium interactions. These facts suggest that the Standard Model is not a complete theory and additional physics Beyond the Standard Model (BSM) is required.

The study of neutrinos is for sure one of the most promising probe to BSM physics and is of vital importance to the future development of particle physics, in particular through precision measurement of their interactions. A deep understanding of neutrino interactions, and neutrino-nucleon interactions in particular, could lead to a great impact on long-baseline experiments, proton decay search, and supernova neutrino detection.

1.1 Neutrino interactions

Neutrinos are colourless and chargeless particles, thus sensitive only to weak interactions. Because of their nature, these leptons have small cross-sections and are difficult to measure. All the interactions are described by the the electroweak part of the SM, based on the symmetry group $\mathrm{SU}(2)_L \otimes \mathrm{U}(1)_Y$, and are governed by the Lagrangian $\mathcal{L} = \mathcal{L}^{(CC)} + \mathcal{L}^{(NC)}$. In fact, neutrinos are mediated by the $W^{\pm}$ for charged-current (CC) interactions and by the Z boson for neutral-current (NC) ones, the Lagrangians of which are as follows:

$$\mathcal{L}^{(CC)} = -\frac{g}{2\sqrt{2}}\left(j^{\mu}_{W,L} W_{\mu} + \mathrm{h.c}\right) \tag{1.2}$$

$$\mathcal{L}^{(NC)} = -\frac{g}{2\cos\vartheta_{\mathrm{W}}} j^{\mu}_{Z,\nu} Z_{\mu}\,, \tag{1.3}$$

where the two currents read

$$j^{\mu}_{W,L} = 2 \sum_{\alpha=e,\mu,\tau} \overline{\nu_{\alpha L}}\gamma^{\mu} l_{\alpha L} \tag{1.4}$$

$$j^{\mu}_{Z,\nu} = \sum_{\alpha=e,\mu,\tau} \overline{\nu_{\alpha L}}\gamma^{\mu} \nu_{\alpha L}\,, \tag{1.5}$$

and $\vartheta_{\mathrm{W}} = 28.7°$ is the Weinberg angle.

The easiest interaction that can be studied is the neutrino-electron elastic scattering

$$\nu_{\alpha} + e^{-} \rightarrow \nu_{\alpha} + e^{-}\,, \tag{1.6}$$

and its antineutrino counterpart. For the electronic neutrino, both CC and NC interactions are allowed, while for $\alpha = \mu, \tau$ the CC interactions are forbidden. The respective Feynman diagrams are shown in Fig. 1.1. The effects of the W and Z propagators can

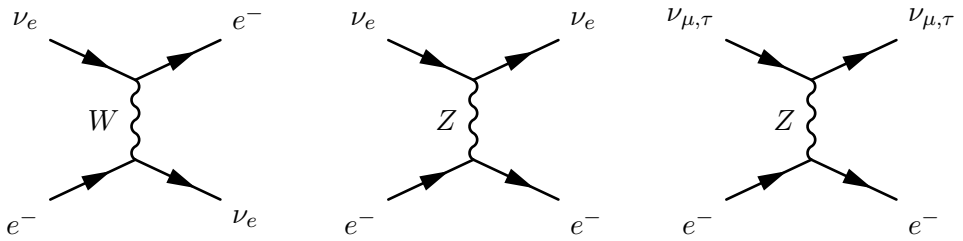

Figure 1.1: The process $\nu_e + e^- \to \nu_e + e^-$ corresponds to the sum of the first two Feynman diagrams. The process $\nu_{\mu,\tau} + e^- \to \nu_{\mu,\tau} + e^-$ is given by the third diagram.

be neglected, for low neutrino energies, and the above processes are described by the effective charged-current and neutral-current Lagrangians

$$\mathcal{L}_{\text{eff}}(\nu_e e^- \to \nu_e e^-) = -\frac{G_F}{\sqrt{2}}[\overline{\nu_e}\gamma^\mu(1-\gamma^5)\nu_e][\bar{e}\gamma_\mu((1+g_V^l) - (1+g_A^l)\gamma^5)e] \tag{1.7}$$

$$\mathcal{L}_{\text{eff}}(\nu_\alpha e^- \to \nu_\alpha e^-) = -\frac{G_F}{\sqrt{2}}[\overline{\nu_\alpha}\gamma^\mu(1-\gamma^5)\nu_\alpha][\bar{e}\gamma_\mu(g_V^l - g_A^l)\gamma^5)e] \quad (\alpha = \mu, \tau)\,. \tag{1.8}$$

The differential cross-section with respect to the momentum transfer Q^2 is the following:

$$\frac{\mathrm{d}\sigma}{\mathrm{d}Q^2} = \frac{G_F^2}{\pi}\left[g_1^2 + g_2^2\left(1 - \frac{Q^2}{2p_\nu \cdot p_e}\right)^2 - g_1 g_2 m_e^2 \frac{Q^2}{2(p_\nu \cdot p_e)^2}\right]. \tag{1.9}$$

The quantities g_1 and g_2 depend on the flavour of the neutrino and related to the vector and axial couplings, g_V and g_A. They read:

$$g_1^{\nu_e} = \frac{1}{2} + \sin^2\vartheta_W \quad , \quad g_2^{\nu_e} = \sin^2\vartheta_W \tag{1.10}$$

$$g_1^{\nu_{\mu,\tau}} = -\frac{1}{2} + \sin^2\vartheta_W \quad , \quad g_2^{\nu_{\mu,\tau}} = \sin^2\vartheta_W\,. \tag{1.11}$$

The differential cross-section as a function of the electron scattering angle in the laboratory frame follows:

$$\begin{aligned}\frac{\mathrm{d}\sigma}{\mathrm{d}\cos\theta} = \sigma_0 \frac{4E_\nu^2(m_e+E_\nu)^2\cos\theta}{\left[(m_e+E_\nu)^2 - E_\nu^2\cos^2\theta\right]^2}\Bigg[g_1^2 + g_2^2\left(1 - \frac{2m_e E_\nu\cos^2\theta}{(m_e+E_\nu)^2 - E_\nu^2\cos^2\theta}\right)^2 \\ - g_1 g_2 \frac{2m_e^2\cos^2\theta}{(m_e+E_\nu)^2 - E_\nu^2\cos^2\theta}\Bigg],\end{aligned} \tag{1.12}$$

where σ_0 reads

$$\sigma_0 = \frac{2G_F^2 m_e^2}{\pi}\,. \tag{1.13}$$

Despite being less straightforward to deal with theoretically, the neutrino interactions with nucleons are easier to study, from an experimental point of view. This is due to the much larger cross-section and a more diverse range of processes. In general, these processes can be categorised according to the momentum transfer. At small Q^2, elastic interactions dominate and may be brought about by both charged and neutral currents. When this occurs via neutral currents, all flavour of neutrinos and anti-neutrinos can scatter off both neutrons and protons in what is referred to as "NC elastic" scattering. The process follows:

$$\nu_l + N \to \nu_l + N\,, \tag{1.14}$$

$$\bar{\nu}_l + N \to \bar{\nu}_l + N\,, \tag{1.15}$$

Once neutrinos acquire sufficient energy they can also undergo the analogous charged current interactions, called "quasi-elastic", due to the fact that the recoiling nucleon might change its charge and mass transfer occurs. The processes read:

$$\nu_l + n \to p + l^- \tag{1.16}$$
$$\bar{\nu}_l + p \to n + l^+ \,, \tag{1.17}$$

with $l = e, \mu, \tau$. For the muonic neutrino with energy below one GeV, the CCQE is the dominant interaction, even though the cross-section plateaus at higher energies, as the available Q^2 increases: it becomes increasingly unlikely for the nucleon to remain intact.

The physics behind the CC quasi-elastic processes is more complicated. The differential cross-sections with respect to Q^2 and to $\cos\theta$ are given in the laboratory frame by:

$$\frac{\mathrm{d}\sigma_{CC}}{\mathrm{d}Q^2} = \frac{G_F^2 |V_{ud}|^2 m_N^4}{8\pi (p_\nu \cdot p_N)^2} \left[A(Q^2) \pm B(Q^2) \frac{s-u}{m_N^2} + C(Q^2) \frac{(s-u)^2}{m_N^4} \right], \tag{1.18}$$

$$\frac{\mathrm{d}\sigma_{CC}}{\mathrm{d}\cos\theta} = - \frac{G_F^2 |V_{ud}|^2 m_N^2}{4\pi} \frac{p_l}{E_\nu} \left[A(Q^2) \pm B(Q^2) \frac{s-u}{m_N^2} + C(Q^2) \frac{(s-u)^2}{m_N^4} \right], \tag{1.19}$$

where the plus sign refers to $N = n$, while the minus sign to $N = p$. The functions $A(Q^2)$, $B(Q^2)$, and $C(Q^2)$ depends on the nucleon form-factors in the following way:

$$\begin{aligned} A = \frac{m_l^2 + Q^2}{m_N^2} \Bigg\{ & \left(1 + \frac{Q^2}{4m_N^2}\right) G_A^2 - \left(1 - \frac{Q^2}{4m_N^2}\right) \left(F_1^2 - \frac{Q^2}{4m_N^2} F_2^2 \right) + \frac{Q^2}{m_N^2} F_1 F_2 \\ & - \frac{m_l^2}{4m_N^2} \left[(F_1 + F_2)^2 + (G_A + 2G_P)^2 - \frac{1}{4} \left(1 + \frac{Q^2}{4m_N^2}\right) G_P^2 \right] \Bigg\} \end{aligned} \tag{1.20}$$

$$B = \frac{Q^2}{m_N^2} G_A (F_1 + F_2) \tag{1.21}$$

$$C = \frac{1}{4} \left(G_A^2 + F_1^2 + \frac{Q^2}{4m_N^2} F_2^2 \right). \tag{1.22}$$

The form factors $F_1(Q^2)$, $F_2(Q^2)$, $G_A(Q^2)$, and $G_P(Q^2)$ are called, respectively, *Dirac*, *Pauli*, *axial*, and *pseudoscalar* weak charged-current form factors of the nucleon. These functions of Q^2 describe the spatial distributions of electric charge and current inside the nucleon and are thus intimately related to its internal structure.

CCQE interactions are particularly important to neutrino physics for mainly two reasons:

- measurements of the differential cross-section in Eq. 1.18 give information on the nucleon form-factors, which are difficult to measure;
- their nature as two-body interactions enable the kinematics to be completely reconstructed, and hence the initial neutrino energy determined which is critical for measuring the oscillation parameters.

In fact, if the target nucleon is at rest, at least compared to the neutrino energy, then this can be calculated as:

$$E_\nu = \frac{m_n E_l + \frac{1}{2}\left(m_p^2 - m_n^2 - m_l^2\right)}{m_n - E_l + p_l \cos\theta_l} \,, \tag{1.23}$$

where the measurement of the momentum, p_l, and the angle with respect to the neutrino of the outgoing charged lepton, θ_l, are only required.

Similar calculations can be made for the NCQE scatterings. The cross-sections have the same form as the CCQE cross-sections in Eq. 1.18 and 1.19, but without the mixing term $|V_{ud}|^2$ and with the proper nucleon form factors. The axial form factor, G_A, can be determined through measurements of the charged-current quasi-elastic scattering processes, because the values of the electromagnetic form factors, F_1 and F_2, are reasonably well known, and the part in Eq. 1.20 containing G_P can be often neglected, thanks to the different mass magnitudes of leptons and nucleons. On the other hand, measurements of the neutral-current elastic scattering cross-section give information on the *strange* form factors of the nucleon, the contribute of which mainly comes from the strange quark [1].

The low Q^2 region also presents an inelastic scattering contribution mostly affected by resonance production, where the nucleon is excited into a baryonic resonance before decaying. Inelastic scattering is dominated at high Q^2 by deep inelastic scattering (DIS), because the neutrino can scatter directly off a constituent quark, fragmenting the original nucleon. In between these extreme scenarios, an additional contribution comes from interactions where the hadronic system is neither completely fragmented nor forms a recognisable resonance. These interactions are referred to as "shallow inelastic scattering", and there is no clear model for dealing with them, by now.

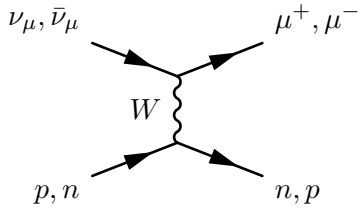

Figure 1.2: Feynman diagram of a CC interaction of a neutrino with a nucleon, which produces the corresponding lepton. This interaction is defined as quasi-elastic.

1.2 Neutrino sources

Numerous are the neutrino sources at the reach of neutrino experiments. Neutrinos are produced in CC interactions, which can happen in nuclear reaction, as for *solar* or *reactor* neutrinos, or in collisions of cosmic rays with the Earth's atmosphere, generating energetic *atmospheric* neutrinos.

Artificial neutrinos can be yielded not only in nuclear reactors, but also in high-energy proton accelerators. Accelerator neutrino beams are fundamental discovery tools in particle physics, in that they allow more control on less parameters. Neutrino beams are derived from the decays of charged π and K mesons, which in turn are created from proton beams striking thick nuclear targets. The precise selection and manipulation of the π/K beam control the energy spectrum and type of neutrino beam. Usually a beam absorber is located at the end of the decay region of an accelerator line, to stop the hadronic and muonic component of the beam, so as to leave an almost pure neutrino beam pointing towards the detector.

The $\pi^\pm$ mesons have a mass of 139.6 MeV and a mean lifetime of 2.6×10^{-8} s. The primary decay mode of a pion, with a branching fraction of 99.99 %, is a leptonic decay into a muon and a muon neutrino:

$$\pi^+ \to \mu^+ + \nu_\mu \qquad (1.24)$$
$$\pi^- \to \mu^- + \bar{\nu}_\mu \qquad (1.25)$$

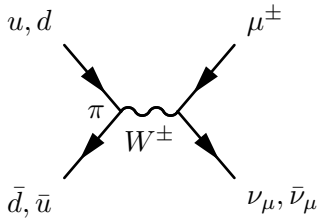

The second most common decay mode of a pion, is the leptonic decay into an electron and the corresponding neutrino, $\pi^\pm \to \nu_e + e$. In spite of the considerable differences in the space momentum, this process is suppressed with respect to the muonic one[1]. The measured branching ratio of the electronic decay is indeed $(1.23 \pm 0.02) \times 10^{-4}$ [7].

The charged kaon mainly decays into a muon and its corresponding neutrino, with a branching ratio of 63.55 %:

$$K^+ \to \mu^+ + \nu_\mu \qquad (1.26)$$
$$K^- \to \mu^- + \bar{\nu}_\mu \qquad (1.27)$$

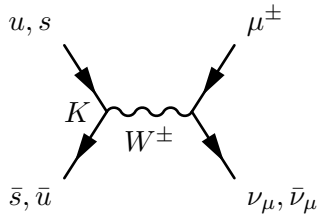

The second most frequent decay (20.66 %) is the decay of the charged kaon into two pions, $K^\pm \to \pi^0 + \pi^\pm$. Other decays have a branching ratio of 5 % or less and are listed in table Tab. 1.1. The decays of the neutral kaon produce neutrino in few cases, instead. The neutral kaon has two mass eigenstates with different lifetimes, the short kaon K_S and the long kaon K_L, because of an oscillation phenomenon caused by the mixing between the two gauge eigenstates, K^0 and $\bar{K}^0$. While K-shorts decay mainly in two pions ($2\pi^0$ or $\pi^+ + \pi^-$), K-longs have a richer variety of final state combination, all of them involving three particles. Among these, neutrinos are produced in the processes:

$$K_L^0 \to \pi^\pm + \mu^\mp + \overset{(-)}{\nu}_\mu \qquad (1.28)$$
$$K_L^0 \to \pi^\pm + e^\mp + \overset{(-)}{\nu}_e \qquad (1.29)$$

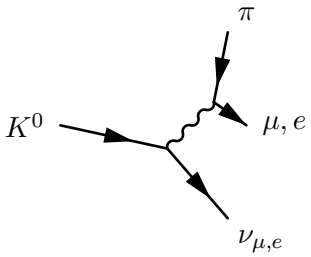

Neutrinos are also produced by muon decay. Muons are unstable elementary particles and decay via the weak interaction. The dominant decay mode, often called *Michel decay*, is also the simplest possible: since lepton numbers must be conserved, one of the product neutrinos of muon decay must be a muonic neutrino and the other an electronic antineutrino; also an electron is produced, because of the charge preservation. Vice versa, an antimuon decay produces the corresponding antiparticles. These two decays are:

[1]This effect is called *helicity suppression* and is due to the great mass of the muon (m_μ = 105.658 MeV) compared to the electron's (m_e = 0.510 MeV); this results in a stronger helicity-chirality correspondence for the electron rather than for the muon. Given that the π mesons are spinless, neutrinos are left-handed, and antineutrinos are right-handed, the muonic channel is preferred because of spin and linear momentum preservation. The suppression of the electronic decay mode with respect to the muonic one is given approximately within radiative corrections by the ratio $R_\pi = \left(\frac{m_e}{m_\mu}\right)^2 \left(\frac{m_\pi^2 - m_e^2}{m_\pi^2 - m_\mu^2}\right) = 1.283 \times 10^{-4}$.

Table 1.1: Decay modes for a charged kaon, $K^{\pm}$, sorted by branching ration (in percent) are listed here.

$\mu^{\pm} + \overset{(-)}{\nu}_{\mu}$	65.55 ± 0.11
$\pi^{\pm} + \pi^0$	20.66 ± 0.08
$\pi^+ + \pi^{\pm} + \pi^-$	5.59 ± 0.04
$\pi^0 + e^{\pm} + \overset{(-)}{\nu}_{e}$	5.07 ± 0.04
$\pi^0 + \mu^{\pm} + \overset{(-)}{\nu}_{\mu}$	3.35 ± 0.03
$\pi^{\pm} + \pi^0 + \pi^0$	1.76 ± 0.02

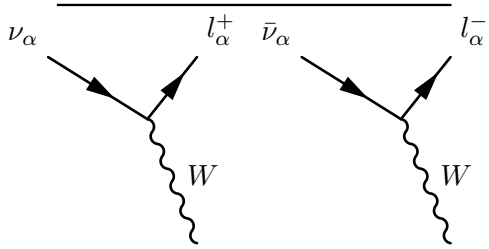

Figure 1.3: Production vertices for neutrinos in CC interactions.

$$\mu^- \to e^- + \bar{\nu}_e + \nu_\mu \qquad (1.30)$$
$$\mu^+ \to e^+ + \nu_e + \bar{\nu}_\mu \qquad (1.31)$$

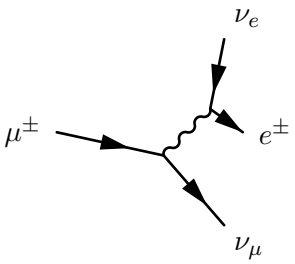

The neutrino source provided by the muon decay is actually more of a nuisance background, because of the long lifetime which gives rise to electronic component in neutrino spectrum.

1.3 Neutrino detection

The study of neutrino is a challenging task, because it is electrically neutral and colourless, and interacts only interact through weak interactions, which has small cross-sections. Its detection thus must rely on weak interactions with matter, where the SU(2) charged counterparts are either produced or scattered by CC or NC interactions, respectively. The physics is mediated by the Lagrangians in Eq. 1.2 and 1.3.

Large active volumes must be employed, such that a significant number of neutrino can be considered and interaction probability is increased. These apparatus are often built underground to shield the detector from cosmic rays and other background radiation. Apart from providing matter to interact with, at the same time these volumes must be capable of detecting the scattered charged leptons. There are many materials or substances that have been be used, such as chlorine, gallium, solid, or liquid scintillators.

One of the most promising techniques is the liquid argon time projection chambers (LArTPC) [8]. As other liquefied noble gases, argon has a high scintillation light yield (50 photons/keV), is transparent to its own scintillation light, and is relatively easy to purify. Compared to xenon, argon is also cheaper and has a distinct scintillation time

profile which allows the separation of electronic recoils from nuclear recoils.

A more dated and better-known technology is the *water Cherenkov* method, where the detector is used to record the Cherenkov light produced when the particles pass through a volume of purified water. Current multi-kiloton scale water Cherenkov detectors, like Super-Kamiokande (SK) [9], have provided many clues in the experimental understanding of the neutrino, produced in solar, atmospheric, or accelerator reactions. However, in spite of the large lifetime of the experiment, some analyses are still limited by statistical uncertainty, which could be overcome with increased exposure. Other analyses suffer from background contamination, as in the case of the supernova relic neutrinos (SRN) search, and would benefit more from the development of new background suppression techniques [10]. This hindrance can be overcome by studying the yield of neutrons in neutrino interactions, such as the *inverse beta decay* (the antineutrino CCQE scattering). It would give a handle on antineutrinos rate, and possibly a method of background reduction for other studies.

1.3.1 Water Cherenkov

The speed of light in vacuum is a universal constant, c, and it is a physical limit of the propagation of information, as stated by the special theory of Relativity. On the contrary, light may travel at speed significantly less than c in a medium. This reduction of speed depends on the relative permittivity of the material, ε, in which light is propagating. Because of the non-zero real part of the dielectric constant, the electromagnetic (EM) field is modified and the phase velocity of light changes from c to

$$v_P = \frac{c}{\sqrt{\varepsilon(\lambda)}} = \frac{c}{n(\lambda)}\,, \tag{1.32}$$

where $n(\lambda) > 1$ is the *refractive index* of the medium and depends on the wavelength (energy) of the propagation wave.

A charged particles moving at a constant velocity in a dielectric medium disrupts the local electromagnetic field, by deforming its molecules and temporarily polarising the material. The dipoles are restored almost instantaneously and thus become impulsive sources of EM waves. If the velocity of the passing particle, $v = \beta c$, is less than the speed of the light in the medium as expressed in Eq. 1.32, i.e. $\beta < 1/n$, then the total energy flux of the excited field is zero and EM waves are not irradiated. On the contrary, if $\beta > 1/n$, the perturbation left by the passage of the particle is such that the energy is released coherently. The result is that the field is different from zero in a cone coaxial with respect to the direction of the charged particle, whose direction is opposite to the particle motion; so the photons are emitted coherently to a fixed angle with respect

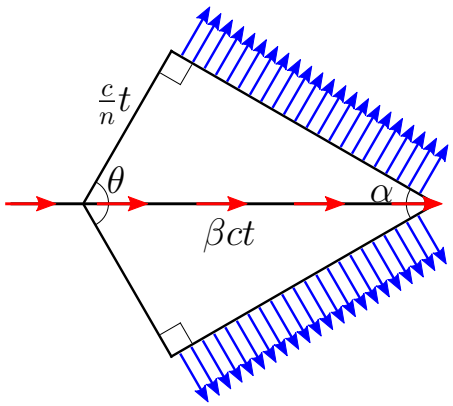

Figure 1.4: A sketch of the geometry of the Cherenkov radiation. The blue arrows represent the emitted photons, the red ones the track of the charged particle. The Cherenkov angle, θ, can be calculated using basic trigonometry.

to the particle motion [11]. With the help of Fig. 1.4, it is easy to find that:

$$\sin\alpha = \frac{1}{\beta n} \tag{1.33}$$

$$\cos\theta = \frac{1}{\beta n}\,. \tag{1.34}$$

where α is the apex angle of the cone and θ is the photon angle with respect to the particle direction. For an ultra-relativistic particle, for which $\beta \sim 1$, there is a maximum angle of emission, given by:

$$\cos\theta_{\mathrm{MAX}} = \frac{1}{n}\,. \tag{1.35}$$

The phenomenon is called *Cherenkov effect*, and it occurs every time a charged particle passes through a dielectric medium with a speed

$$\beta > \frac{1}{n}\,. \tag{1.36}$$

The condition can also be expressed in terms of the particle energy, given that $E^2 = p^2 + m^2$ and $\beta = p/E^2$. The threshold becomes:

$$\frac{E}{m} > \frac{1}{\sqrt{1-1/n^2}}\,, \tag{1.37}$$

with m the mass of the charged particle. According to the theory of electromagnetic waves, a charged particle moving uniformly does not irradiate and this proves that the Cherenkov radiation is not related with Bremsstrahlung. The radiation is emitted in the visible and near visible regions of the EM spectrum, but also as radio and microwaves. A real medium is always dispersive and radiation is restricted to those frequencies bands for which $n(\nu) > \frac{1}{\beta}$. In the x-ray region, for instance, $n(\nu)$ is always less than one and radiation is forbidden at this energies, because Eq. 1.36 cannot be satisfied. Truly, coherent emission of light needs two more conditions to be fulfilled:

- the length of the track of the particle in the medium should be large compared with the wavelength, λ, of the radiation in question, otherwise diffraction effects will become dominant;
- the velocity of the particle must be constant during its passage through the medium, or, to be more specific, the differences in the times for particle to traverse successive λ distances should be small compared with the period $\frac{\lambda}{c}$ of the emitted light [12].

The number of photons emitted by a charged particle of charge Ze per unit path length and per unit energy interval, or equivalently to λ, of the photons is equal to:

$$\frac{\mathrm{d}^2N}{\mathrm{d}x\mathrm{d}\lambda} = \frac{2\pi\alpha Z^2}{\lambda^2}\left(1 - \frac{1}{\beta^2 n^2(\lambda)}\right). \tag{1.38}$$

This means that the greater part of Cherenkov photons are emitted in the ultraviolet range, because of the proportionality to $1/\lambda^2$.

Cherenkov detectors take advantage of this effect, detecting the light produced by charged particles. A large volume of transparent material, such as water, ice, or liquid scintillator, can be surrounded by photosensitive detectors in order to capture the

[2]For this calculation, the convention $c = 1$ is adopted.

Cherenkov radiation. This technique is largely used in neutrino experiments, where the charged lepton, yielded in CC or NC interactions, is observed. It is possible to reconstruct information on the interaction from the intensity and geometrical distribution of the light collected, such as the velocity of the charged particle, which is related to the energy of the incident neutrino, or the position of the interaction vertex. Not every neutrino energy allows the production of a charged lepton, due to the Cherenkov threshold, but only MeV-scale neutrinos can be observed in a Cherenkov detector[3]. When the velocity of the charged lepton drops under the threshold, the light is detected on a surface in the shape of a ring, from which further information can be inferred.

1.3.2 Gadolinium neutron capture

Neutrons are chargeless and cannot interact with matter by means of the Coulomb force, which dominates the energy loss mechanisms for charged particles, described by the Bethe formula. Neutrons can interact with nuclei in various other ways, depending on the energy:

- elastic and inelastic scattering;
- transmutation;
- neutron activation;
- spallation reaction;
- neutron-induced fission;

As a result of the interaction, the neutron may either be absorbed or change its energy and direction significantly. In this way the average energy of a neutron beam can be completely or partly reduced up to thermal energies (*thermalisation*), close to $k_{\mathrm{B}}\,T$ (0.025 eV) and below. Neutrons present in this range of energy a different and generally much larger effective neutron absorption cross-section for a given nuclide, compared to, for instance, fast neutrons. Thermalisation can result in a *neutron activation* process in which atomic nuclei capture free thermal neutrons, creating heavier nuclei, often in an excited state; the excited nucleus decays almost instantaneously emitting usually gamma rays.

The thermalisation of neutrons follows an exponential distribution of time . The time constant in water is frequently measured and is found to be $\sim 5\ \mu$s [13] [14]. Neutrons can be captured either by hydrogen nuclei or, less likely, by oxygen nuclei. Hydrogen requires a double capture to become unstable (tritium), while oxygen must capture three neutrons to become oxygen-19. The hydrogen capture is hard to study because the energy released by the compound nucleus is very low, around 2.2 MeV, and sometimes this signal could be mixed with background. In SK, for instance, this gamma would result in about seven photo-electrons, and thus only detectable with $\sim$20 % efficiency [15].

Gadolinium-157 has the highest thermal neutron capture cross-section among any stable nuclide, greater than 2.2×10^5 barns, while gadolinium-155 has a cross-section greater than 6×10^4 barns [16]. Dissolving gadolinium compounds in water could considerably increase the neutron capture probability, from 0.3 barns in pure water (free protons) to, for instance, 4.9×10^4 barns with by adding only 0.2 % of $GdCl_3$ [17]. Neutrons in water thermalise quickly and can thus be captured by a Gd nucleus with a

[3]For instance, the CCQE process $\bar{\nu}_e + p \rightarrow n + e^+$ has a energy threshold of 1.81 MeV and the interaction $\nu_\mu + n \rightarrow p + \mu^-$ has the threshold of 110.16 MeV, because of the muon mass.

probability of 90 %. The most probable processes follow:

$$n_{\text{th}} + {}^{155}\text{Gd} \rightarrow {}^{156}\text{Gd}^{*} \rightarrow {}^{156}\text{Gd} + 8.5 \text{ MeV}\,; \tag{1.39}$$

$$n_{\text{th}} + {}^{157}\text{Gd} \rightarrow {}^{158}\text{Gd}^{*} \rightarrow {}^{158}\text{Gd} + 7.9 \text{ MeV}\,. \tag{1.40}$$

When one of these occurs, three or four gammas are emitted and a cascade is produced, giving enough light to locate the capture vertex. These processes have a temporal ($\sim$ 30 μs) and a spatial coincidence ($\sim$ 4 cm) with the lepton coming from the initial interaction, in opposition with hydrogen capture which happens roughly 10 times slower. It is then possible to significantly reduce the backgrounds, since even moderately energetic neutrons, ranging from tens to hundreds of MeV will quickly lose energy by collisions with free protons and oxygen nuclei in water.

Chapter 2

The ANNIE Experiment

As more neutrino data become available, lack of knowledge of the fine details of neutrino-nucleus interactions begins to limit the physics reach of future experiments. For instance, final-state neutron abundance from pure neutrino interactions is currently poorly known and difficult to measure. Data on neutron yield in relation to energy and direction of final-state muons can be used to better constrain nuclear models of neutrino interaction physics and are an essential input for Monte Carlo models, used for calculating detection efficiencies, expected background rates, accurate limits, and confidence levels. The count of neutrons can also be used to reject contamination by atmospheric neutrino interactions in proton decay experiments and in a sample of diffuse supernova background neutrinos, as well as wrong-sign contamination in oscillation analyses. In addition to helping understand fundamental neutrino-interaction physics, tagging events by the presence and number of final-state neutrons can provide physics analyses with a better handle for signal/background separation and even allow for discrimination between different types of neutrino interactions.

Figure 2.1: Logo of the ANNIE experiment.

A study of final-state neutron abundance can be accomplished by the **A**ccelerator **N**eutrino **N**eutron **I**nteraction **E**xperiment (ANNIE), which will provide a complementary measurement of neutron yields in neutrino-nucleon interactions [18]. The ANNIE experiment is a prototype neutrino detector currently taking data at the Fermi National Accelerator Laboratory (FNAL), in Chicago, USA. It consists of a small water Cherenkov detector, placed at the former location of the SciBooNE experiment [19] and deployed on the intense Booster Neutrino Beam (BNB). An upstream forward Veto and a downstream Muon Range Detector (MRD) are also installed in the hall. The experiment aims to be a test bed for many new technologies, such as the gadolinium-doped water and the use of early prototype Large Area Picosecond Photodetectors (LAPPDs). The ANNIE experiment will be an innovative application of these devices demonstrating their feasibility for Water Cherenkov neutrino detectors.

The experiment is planned to proceed in two main stages, spread over five years:

phase I a partially-instrumented test-beam run using only Photomultipliers (PMTs) for the purpose of measuring critical neutron backgrounds to the experiment;

phase II a longer run with a more instrumented detector where incremental research

and development for the LAPPDs and purpose-built fast electronics will be fulfilled, as well as the improvement of the required photodetector coverage (both LAPPDs and PMTs).

Year 1 will focus on the R&D, particularly on the development of the Data Acquisition system, along with the testing in water of the first model of LAPPD. Installation of the first LAPPDs, a significant fraction of the additional PMTs, and as the calibration system, will take place in *Year 2*. Data-taking would commence in *Year 3* and continue through *Year 5*, with the physics reach of the detector improving as the fraction of LAPPDs increases over time.

This thesis is placed at the beginning of *Year 1*, where the experimental setup of phase I is tested and R&D is undertaken.

2.1 Physics of the experiment

Aside from the opportunity to test new technologies, ANNIE will also collect valuable data by observing interactions between neutrinos and nucleons. Little is known about the Physics behind these processes, except from that it is strictly influenced by the complex interplay of multiple particles.

The principal process at first order, that the experiment is sensitive to, is the charged current quasi-elastic scattering of the muon neutrino on a bound nucleon (see section 1.1); the interaction yields a proton (neutron) from the neutrino (anti-neutrino) interaction. CC scattering without pions in the final state is a critical component for neutrino oscillation experiments [20]. However, CCQE cross section precise measurements have been unavailable, for several reasons:

- neutrino beams typically span a wide energy range thereby preventing an incoming energy constraint on the reaction;
- the neutrino flux itself is often poorly known, hampering normalisation of reaction rates;
- background processes are frequently significant and difficult or impossible to separate from the CCQE signal;
- the target nucleon is not free but bound in a nucleus and correlations between nucleons are important.

The theory describing these interactions is still under development and is often weakly constrained by the available data [21]. Higher-order processes and multi-scale nuclear physics, including secondary p/n scattering of struck nucleons within the nucleus, charge exchange reactions of energetic hadrons in the nucleus (e.g., $\pi^- p \to n\pi^0$), and Meson Exchange Currents (MEC) [22], where the neutrino interacts with a correlated pair of nucleons, all modify theoretical expectations.

The MiniBooNE experiment [23] has been able to measure the double differential cross section for the CCQE interactions of muon neutrinos [24] and antineutrinos [25], on a carbon-12 target. In the framework of a modified Real Fermi Gas model [26], the axial mass, M_A, of the dipole axial form factor was measured to be greater than older measures. Within the model prediction, a larger value for M_A implies a larger cross section, because the CCQE cross section increases approximately linearly with the axial mass. This may indicate a significant contribution from neglected mechanisms for CCQE-like scattering from a nucleus such as multi-nucleon processes. For instance, the

double differential cross section for CCQE interactions is better described by models including *two-body currents*, where low-energy neutrinos scatter off correlated pairs of nucleons. Several models [27] [28] have been developed on two body currents, but there is no consensus on many details how these events look like.

A model-independent consequence of two-body currents is higher multiplicity of final state neutrons, therefore the number and type of nucleons ejected from the interaction would be a key handle in understanding neutrino-nucleus interaction- As stated before, detection of neutrons from nuclear interactions would have a transformative impact on a wide variety of neutrino physics measurements. Nevertheless there are major limitations on the effective execution of neutron tagging techniques, in both sides of Physics:

- theoretically, there are still large uncertainties on models of the nuclear mechanisms that produce neutrons in GeV-scale neutrino interactions;
- experimentally, the neutron yield hasn't been satisfactorily measured yet.

ANNIE can study neutron yields from mostly-pure neutrino interactions separately, by measuring neutron production in relation to the energy and direction of final-state muons with respect to the original neutrino. The search for a delayed signal from neutron capture by gadolinium salts dissolved in water is a promising technique for detecting final state neutrons [10]. The probability of producing zero, one, or multiple neutrons from a neutrino interaction must be characterised, as a function of both interaction type and momentum transfer. This evaluation is expected to require orders of ten thousands neutrino interactions, which should be around 10 % of the interactions in the detector considering the efficiencies and acceptances of the experimental setup. This corresponds to one year of data with the detector fully instrumented. the more demanding goal of studying neutron yields for specific event classes can be met, with additional statistics and improved detector performance.

A precise evaluation of the neutron production requires a high efficiency measure and event reconstruction. The experiment relies on the detection of Cherenkov light, produced by charged particles yielded in neutrino interactions. For this reason the photocoverage should be wisely optimised. It is possible to estimate the number of photons produced by the Cherenkov effect, starting from Eq. 1.38. Its integration with respect to space and wavelength, λ, returns:

$$N = 2L\pi\alpha Z^2 \int_{\lambda_2}^{\lambda_1} \frac{1}{\lambda^2}\left(1 - \frac{1}{\beta^2 n^2(\lambda)}\right)\mathrm{d}\lambda\,. \tag{2.1}$$

If the λ dependence of the refractive index is negligible, the formula for an ultra-relativistic charged lepton becomes:

$$N = 2L\pi\alpha \sin^2\theta_C\left(\frac{1}{\lambda_1} - \frac{1}{\lambda_2}\right). \tag{2.2}$$

For example, it is possible to roughly estimate the number of photons detected to the passage of a muon in ANNIE's water volume ($L = 4$ m). The quantum efficiency of most PMTs peaks around 20 % in the spectrum that spans from 300 nm to 500 nm. Since $\theta_C = 41°$, the detectable photons are

$$N \simeq 2.1 \times 10^4\,. \tag{2.3}$$

Geometry effects can significantly modify this result, as well as reflection of the walls.

The sizes of ANNIE are reduced compared to other water Cherenkov detectors. The difference in transit time between two photons arriving at the same photosensor from two different forward-pointing tracks is merely few nanoseconds. Such delays are not a hindrance for data analysis. Handling afterpulsing signals and delays due to light reflection could be more cumbersome, instead, event though. the knowledge of their time properties helps the discrimination. For example, a "late pulse" occurs after three times the transit time of the photoelectron in the PMT (generally between 30 ns and 150 ns), while the "after pulse" can happen much later (from 100 ns to 15 μs) than the main pulse[1]. Light reflection effects are constrained to the geometrical features of the tank, instead.

2.2 Neutrino beam

ANNIE is run on axis from the *Booster Neutrino Beam* (BNB), which deploys 8.89 GeV protons accelerated by the FNAL booster operating at 15 Hz. Selected batches containing approximately 5×10^{12} protons are extracted and bent toward a beryllium target via dipole magnets. Each spill is composed of 81 bunches of protons, approximately 6 ns wide each and 19 ns apart, for a total spill duration of 1.6 μs. The detector expects the neutrino beam to arrive with a spill frequency of 15 Hz, divided in pulse trains, around 1 s apart each other [29]. The BNB is dealt in detail in the appendix A. A resistive wall monitor (RWM) generates a logic signal at every intensity peak, which can be used to trigger the experiment in correspondence of each spill. The distance between the centre of the beryllium target and the centre of the hall is taken to be 99.9 m, with the detector located on beam axis within a tolerance of a few centimetres [29].

The predictions on the neutrino flux are the same as the one produced by the SciBooNE collaboration [19], obtained via a GEANT4-based beam Monte Carlo simulation. The simulation code developed by the MiniBooNE Collaboration is used [24], where a realistic description of the geometry and materials present in the BNB target hall and decay region is used. The interactions of primary protons with the beryllium target are simulated according to state-of-the-art hadron interaction data. Particles emanating from the primary interaction in the target are then propagated within the GEANT4 framework, which accounts for all relevant physics processes. A second, FORTRAN-based Monte Carlo code is responsible for generating the neutrino kinematics distributions from meson and muon decays, and for obtaining the final neutrino fluxes extrapolated to the detector hall with negligible beam Monte Carlo statistical errors. Once produced by the simulation, neutrinos are extrapolated along straight lines toward the detector and all neutrinos, the traces

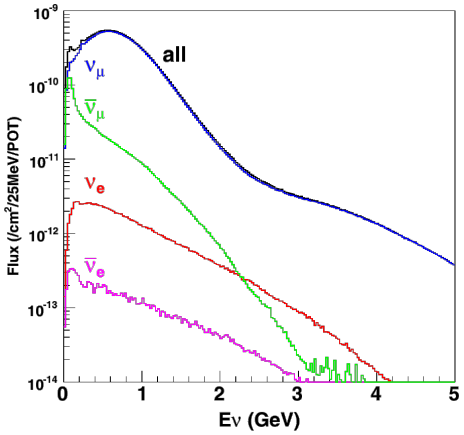

Figure 2.2: Neutrino flux predictions from the GEANT4/FORTRAN simulation. The spectrum peaks in the 700 MeV region. Figure taken from [19].

[1]The late pulse is caused by the back scattering of the photoelectrons on the first dynode without multiplication. The after pulse is provoked by residual ionisation in the vacuum tube which produces an additional photoelectron.

of which cross any part of the active volume, are considered for the flux predictions. The neutrino flux prediction at the detector location as a function of neutrino energy is shown in Fig. 2.2. A total neutrino flux per proton on target of 2.2×10^{-8} cm^{-2} is expected at the hall location and in neutrino running mode (positive horn polarity), with a mean neutrino energy of 0.7 GeV. The flux is dominated by muon neutrinos (93 % of total), with small contributions from muon antineutrinos (6.4 %), and electron neutrinos and antineutrinos (0.6 % in total). The projected number of protons incident on the target (POT) per year for the BNB is about 2×10^{20} POT. The rates expected per year when running in neutrino mode for one ton of water are about sixteen thousands neutrino interactions, where eleven thousands of those would be ν_μ CC interactions. The neutrino interactions occur in the tank approximately every 150 spills of 4×10^{12} POTs. Additional simulations suggest that an externally generated muon enters the tank once every ∼195 spills. These rates are ideal as they ensure single neutrino interactions in the detector.

2.3 The Hall

The experiment is set up in the former site of the SciBooNE experiment, located 8 m below the surface and the 100 m from the BNB target [30]. Already existing instrumentation in the hall, such as some PMTs and the MRD, is borrowed by the ANNIE experiment.

2.3.1 Water tank

The main component of the experiment is the water tank, built and installed in the hall. It consists of a welded steel water tank, with dimensions 10 ft (slightly more than three metres) of diameter per 13 ft (about four metres) of height, enclosing roughly 23 tonnes of water. The diagonal of the cylinder, which is the longest path inside the tank, is about five meters long. It corresponds to about seventeen light-nanoseconds. The inner volume is lined with 40 mil white PVC (87 % light reflection) and is outfitted with a inner support structure capable of ultimately housing several hundred photosensors. Sixty PMTs are already installed on the bottom of the volume. The tank is filled with pure water, but ANNIE's water transparency requirements are less stringent, thanks to its two orders of magnitude smaller volume than Super-Kamiokande: ANNIE needs only to keep a transparency of about 25 meters to lose less than 10 % of the light, as opposed to SK's effective water attenuation length of 90 meters. The water volume also requires a source of dry nitrogen in order to suppress the growth of biologics in the water. This nitrogen is bubbled through the water during fill and afterwards a blanket of nitrogen is maintained above the surface of the water. The recirculation is kept as low as necessary to maintain a pure N_2 environment. ANNIE also relies on the plastic

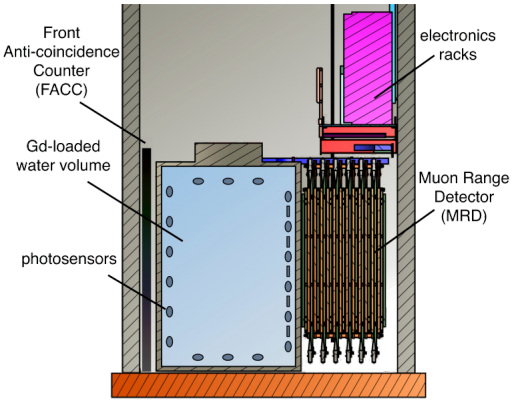

Figure 2.3: Schematic of the experimental hall. The neutrino beam propagates from left to right.

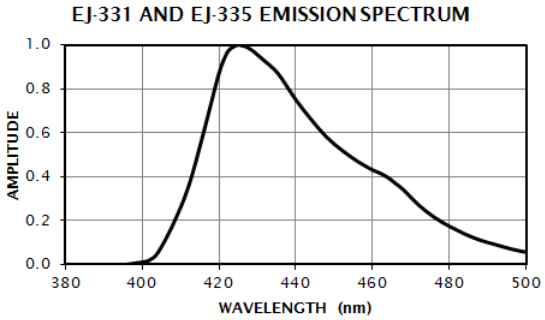

Figure 2.4: EJ-335 emission spectrum. This scintillator contains mineral oil substituted for some of the aromatic solvent for purposes of higher hydrogen content and higher flash point for use in very large tanks. The gadolinium content is 0.25% by weight. The wavelength of peak emission is 424 nm.

liner to prevent ions, that might compromise transparency, from leaching into the water from the tank walls. Water quality is supposed to be monitored using the detected light intensity from cosmic ray muons.

A concentrated solution of high-quality (99.99% TREO[2]) gadolinium sulphate $Gd_2(SO_4)_3$ will be mixed in a portable polypropylene barrel with pure water. The available 50 kg of Gd are enough for one test loading (4 kg) and one full loading (40 kg), with 6 kg left over for various other studies and tests. Thanks to the complex water recirculation system, the Gd-loaded water can be removed and stored in a secondary tank, then returned and repurified with minimal loss of Gd, between ANNIE's runs. Upon completion of the experiment the gadolinium can be easily recovered using a portable demineraliser. Measurement of neutron background are possible due to the neutron volume capture (NCV), a small vessel located inside the tank. It consist of a 50 cm $\times$ 50 cm transparent acrylic cylinder, with 2.5 cm thick walls. The vessel contains 100 L of Gd-doped EJ-335 liquid scintillator, specialised for neutron detection, and can be moved inside the tank. The scintillator light emission is 55 % of the anthracene output, which is 1.6×10^4 photons/MeV. The light spectrum is shown in Fig. 2.4. From [31], around 2×10^2 photons are expected from neutron capture in liquid scintillator. With the NCV geometry in mind, nearly a tenth of them can be observed by a PMT mounted on top of the vessel, whereas about a sixth of the photons should be captured by the detectors on the bottom. The vessel is weighted so as to have a negative buoyancy. Position dependence of the neutron rates from different overburdens of water can be studied by raising and lowering the NCV and translating it along the beam axis.

2.3.2 Photodetectors

The core of the experiment is the Cherenkov light detection. The coverage provided by 60 8″ PMTs borrowed from the WATCHBOY experiment [32] is enough for phase I. The photomultipliers are mounted in a frame on the bottom of the tank, facing upward. The frame is designed to support both the weight of the phototubes in gravity as well as the buoyant forces in water. The detectors, immersed in water, are operated at a positive high-voltage (HV), with a single cable for both power and signal. The water acts as ground and the employed voltages could lead to electrical breakdown through the glass of the PMT, if a negative voltage is applied to the cathode. Supplying a positive

[2]TREO expresses the Total Rare Earth Oxide percentage in the element.

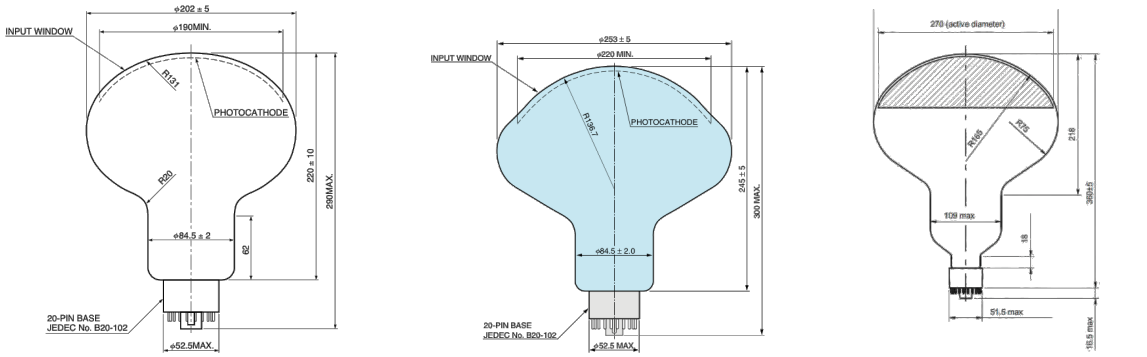

(a) 8″ Hamamatsu R5912. **(b)** 10″Hamamatsu HQE R7081. **(c)** 11″ ETEL D748KFLB.

Figure 2.5: Schematic of the PMTs selected for the experiment.

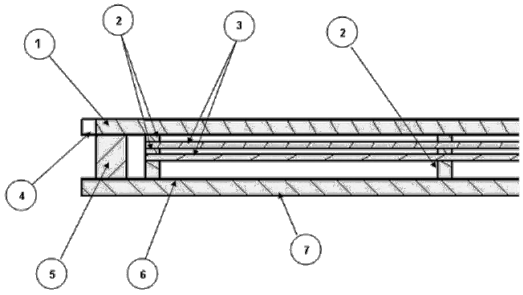

Figure 2.6: The basic structure of the LAPPD detector. The sealed vacuum tube consists of a top window with the photocathode on the inner surface (1), an accelerating gap for the initial photo-electron (2), a pair of 20-cm-square MCPs in a Cherenkov geometry that amplify the photo-electron by factors up to 5×10^7 (3), a gap after the output of the second MCP (2), and the anode that collects the exiting electrons (6). The package is less than 15 mm thick.

voltage to the anode, instead, helps to avoid this issue, since the cathode is set to ground. Capacitors are required to filter the signal from the power supply voltage.

As noted earlier, the necessary photo-coverage to reconstruct events in water will be achieved in ANNIE phase II by a set of PMTs, schematised in Fig. 2.5:

- reusing the 8″ Hamamatsu PMTs recovered from ANNIE phase I.
- purchasing new High Quantum Efficiency (HQE) 10″ Hamamatsu PMTs;
- employing refurbished 11″ Electron Tubes Enterprise PMTs [33].

A series of simulations has been run with different sizes and numbers of PMTs, In order to determine the necessary photocathode coverage. These simulations consider neutron captures on both Gd (90 %) and the hydrogen from the water (10 %). After cost and availability are taken into account, it is found that the detection can be optimised by using 58 8″ tubes, 20 11″ tubes, and 45 HQE 10″ tubes. Gadolinium captures typically produce several photons, therefore the probability of observing enough hits to detect the event is related to the number of photoelectrons produced. This number is strictly correlated with the number of hits. The predictions agree well with a simple scaling argument based on measurements at Super-Kamiokande. Using the planned mix of 11″ tubes, 8″ tubes, and HQE 10″ tubes, it is found that 5 (good correlation) and 10 (strong correlation) photoelectrons are produced respectively 99 % and 94 % of the time.

The use of advanced, high resolution photodetectors, in addition to the PMT coverage improvement, could have a transformative impact on future neutrino detectors

relying on light collection, in particular for precise vertex reconstruction. The most promising technology, selected for ANNIE, is the Large Area Picosecond Photodetector (LAPPD), a microchannel plate (MCP) based photomultiplier. Using the atomic layer deposition (ALD) technique[3], it is possible to produce large-format MCP detector systems by conformally coating inactive, micro-pore glass substrates. The technique allows for the independent optimisation of the geometric, resistive, and secondary electron emission properties of the channel plates. The final detector can achieve single photoelectron time resolutions less than 100 ps and spatial imaging capabilities to within a single centimetre. This provides a much crisper detection of the Cherenkov radiation edge and greatly improves the ability to distinguish between closely separate rings, compared to PMTs which have time resolution in nanoseconds and act as a single pixel, despite the large active area. The combination of LAPPDs and PMTs allows the full detector to work as a tracking detector, with track and vertex reconstruction approaching size scales of just a few centimetres. It also favours the reconstruction of events very close to the wall of the detector, thanks to the small thickness of the LAPPDs (less than 1.5 cm); thus, the fiducial volume is maximised. The LAPPD capabilities also translate into better energy resolution and better discrimination between dark noise and photons from neutron captures. Large Monte Carlo ensembles show that photon pileup on LAPPDs is low enough that only one or two hist per channel are typically visible, so each photon can be individually measured. Preliminary studies show that 20 LAPPDs can provide sufficient coverage and have well-suited performance characteristics for addressing the challenges of water Cherenkov reconstruction in a small volume. Better reconstruction could be possible as larger numbers of LAPPDs become available. Reaching a 10 % isotropic coverage would not only allow the identification of multi-track events, but also the constituent particles and the exact topology, thus potentially expanding the physics reach of the experiment.

2.3.3 Veto system and Muon Range Detector

ANNIE is composed of two more detectors other than the water tank in the hall: a veto system and a muon detector.

The veto is provided by a Forward Anti-Coincidence Counter (FACC) consisting of two layers of overlapping paddles of plastic scintillator. Each layer employs 13 paddles to detect charged particles produced in the dirt upstream of the hall or muons from the BNB, which hasn't decayed. This allows the rejection of events in the tank unrelated to neutrino interactions. Two-inches PMTs read the signals from the scintillator.

An iron-scintillator sandwich, inherited from the SciBooNE experiment, is also present in the hall. The Muon Range Detector (MRD) is used to range out and fit the direction of daughter muons produced by CCQE interactions in the water target. It is not magnetised, thereby discerning particles from antiparticles is not possible. The MRD is designed to measure the momentum of muons up to 1.2 GeV/c using the range measurement. Muon's energy reconstruction could give a handle on the neutrino energy. Its schematic is shown in Fig. 2.7. It consists of 12 iron plates and 13 alternating horizontal and vertical plastic scintillator planes. Each iron plate is 5 cm thick, and covers an area of (274×305) cm^2. The total mass of absorber material is approximately 48 tonnes, while the detector weighs about sixty tonnes. The density of a spare iron plate has been measured at several positions of the plate, to be 7.841 ± 0.002 g/cm^3 [35]. Each

[3]ALD [34] is a thin film deposition technique that is based on the sequential use of a gas phase chemical process. The process is based on binary reaction sequences where two surface reactions occur and deposit a thin binary compound film.

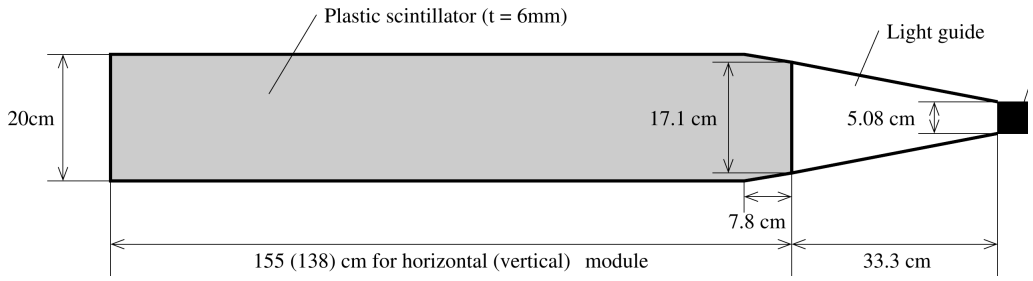

Figure 2.8: Scintillating paddle used for the MRD. Figure taken from [35].

scintillator plane consists of 20 cm wide, 6 mm thick scintillator paddles, as illustrated in Fig. 2.8. Each vertical plane is comprised of 138 cm long paddles, arranged in a 2×15 array to have an active area of 276×300 cm^2. On the other hand, each horizontal scintillator plane consists of 155 cm long paddles, arranged in a 13×2 array to have an active area of (260×310) cm^2. In total, 362 paddles, 182 vertical and 180 horizontal, are used in the MRD. The scintillator paddles are read out by five types of 2″ PMTs[4]. The photomultipliers of the horizontal modules have 14 stage dynodes, whereas those used for vertical modules have 10 stage dynodes, hence the PMTs used for the vertical planes have relatively low gain and efficiency compared to that used or horizontal planes. To ensure the same efficiencies, the vertical modules are amplified by the factor of 10 using LeCroy 612 fast amplifiers. This choice is forced by space limitations [36],

As far as the electronics are concerned, the FACC and MRD are essentially similar, in that both detectors are composed of scintillating paddles and small phototubes, and they follow the same rectilinear geometry. The veto has two layers of 13 horizontal scintillators, and, in phase I, only two layers of the MRD are operative: one vertical and one horizontal (the second and the third layers, respectively). *Layer 2* consists of two sets of 13 horizontal paddles, while *Layer 3* consists of two sets of 15 paddles. The number of needed readout channels from these two subsystems are

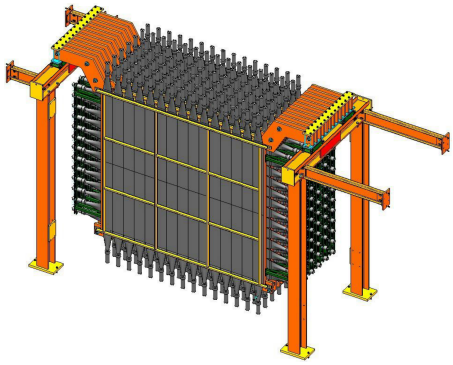

Figure 2.7: Drawing of the MRD. Figure taken from [35].

- 26 channels for the forward Veto;
- 26 channels for *Layer 2* of the MRD;
- 30 channels for *Layer 3* of the MRD;

for a total of 82 channels, which are addressed by CAMAC electronics (see section 3.2.1). In place of the full CAMAC electronics implementation, the signals from the two detectors are summed and read by the VME electronics (section 3.1.1) to give a first handle on these devices.

[4]The vertical planes use Hamamatsu 2154-05 and RCA 6342A PMTs; the horizontal planes use of EMI 9954KB, EMI 9839b and 9939b PMTs.

Chapter 3

Data Acquisition system

Modern high energy physics experiments require automated procedures to collect data from detectors and save them in long term storage for following analysis. These routines are gathered in automated system called data acquisition systems (DAQ), which typically include three fundamental components:

1. sensors, to convert physical parameters to electrical signals;

2. signal conditioning circuitry, to convert sensor signals into a form that can be converted to digital values.

3. conversion from analog signals to digital values and subsequent storage.

The last step is vital in that it allows data manipulation and analysis by a computer.

As far as ANNIE is concerned, the first requirement has already been discussed in section 2.3: the experiment has multiple simultaneous data sources, which are the forward veto, the water PMTs and the MRD, as well as a blend of front-end electronics technologies (VME, CAMAC and custom FADCs) for waveform and time digitisation. Considering this variety of devices, the whole system has also some requirements to achieve:

- stability, on long acquisition runs;
- calibration;
- real time online monitoring;
- direct and remote user control.

Provided a robust electronic system, these tasks are thoroughly accomplished on the software's side, since the system is based upon the *ToolDAQ Framework*, developed by Dr Benjamin Richards [37] for the Hyper-Kamiokande collaboration (HK). The HK group has used this opportunity to undertake R&D and testing of DAQ software and tools for future use in the HK experiment. ANNIE has allowed extensive testing of the flexibility of the software and all the above features to take place within a single deployment. ToolDAQ is designed to incorporate the best features of other frameworks, and it allows to easily develop DAQ implementations in a modular way. It can also be employed on large scale experiment, thanks to its scalable network infrastructure, provided by a service discovery protocol.

The main executable relies on user-defined modular classes, called *Tools*, which present three principal functions: *Initialise*, *Execute*, and *Finalise*. The Tools can be daisy-chained to a *ToolChain* and then handled sequentially by the software whenever one of the functions is called. Parameters, data and other variables are passed between Tools by an editable shared data class, which each tool is allowed to read, update, and modify. The ToolChain also manages the more complicated aspects of the DAQ system, like the remote control, the service discovery, and the status of the Tools. The bare structure is sketched in Fig. 3.1.

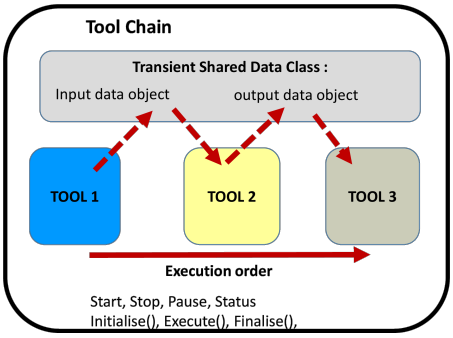

Figure 3.1: Schematic of a ToolChain. The Tools are allowed to communicate with a shared data class, which belongs to the ToolChain.

In the following sections, the whole DAQ structure is delineated as it currently is, i.e. composed of three parallel ToolChains: the Main DAQ Chain, the VME Chain, and the CAMAC/MRD Chain. The latter hasn't been implemented in the Main DAQ system yet, which is composed by the first two Chains only. At the moment the MRD Chain is employed as a standalone DAQ, working aside to the Main DAQ, on a different CPU with understandable difficulties. Ways of overcoming this issues and future integration of the two DAQ in the same machine are eventually discussed.

3.1 Main DAQ Chain and VME Chain

3.1.1 Hardware

The primary readout for ANNIE phase I is provided by a VME-based system[1] developed for the KOTO experiment [39] by University of Chicago. The crates are governed by a VME-based CPU board, interfaced with an Internet Rack Monitor system (IRM) of Fermilab, which allows network connection and supports internet protocols that manage data request and setting access, all based upon the User Datagram Protocol (UDP) transport layer.

The system consists of two types of VME module:

- custom fast analog-to-digital converters (FADC), with 500 MHz sampling pipeline, 14 bit resolution, and four channels;
- Master Trigger (MT) cards which distribute a 125 MHz clock, synchronises the FADC cards, and provides the trigger.

The leading edge of photomultiplier signal is too fast for an 8 ns (125 MHz) sampling. To reduce dead time and allow the 500 MHz sampling, the digitised signals from the detectors are sent to 8000 samples long pipelines, managed by a Field Programmable Gate Array (FPGA), until a trigger decision is made. The trigger system uses the waveform information with increased sophistication on three levels. Each MT card can

[1]The *VMEbus* is a data transfer architecture, where "VME" stands for VERSA Module Eurocard. It is widely used in High Energy Physics due to the fact that it is of public domain and its data transfer speed is fast: for instance the latest manifestation, the VME320/2eSST protocol, can double the theoretical bandwidth of VME to 320MB/s [38].

address 8 FADC cards, but can also be daisy-chained or arranged hierarchically to address more cards. Given the 16 FADC cards of the ANNIE readout, 3 MT cards are used: one Level-0 card distributes the clock between two Level-1 MT cards, each addressing 8 FADCs. A down-sampling to 125 MHz was established for storage limitations. The resolution of 8 ns suffices the needs of the R&D stage of phase I. Given that 80 μs long time windows are collected, four data sets can be hold in the 40000 samples buffer, using this time resolution. Each set corresponds to a spill from the beam.

The system primarily records the traces from the water PMTs. The MRD and the veto rely on the same FADC system, but the signals from the scintillating paddles are combined through an analog OR and sent to spare FADC channels on the KOTO boards.

3.1.2 Software

The data from the water PMTs and the logical sum of the Veto and MRD are acquired by the Main DAQ, which hinges upon two strictly complementary ToolChains: the Main Chain and the VME Chain. The Main Chain is the primary ToolChain of the DAQ system, which communicates with the other two processes.

The tools of the Chain are schematised in Fig. 3.2 and have the following tools:

Main DAQ	**VME**
Input variables	
PostSQL	VME Trigger Send
Trigger	Board Reader
Network Receive Data	Network Send Data
Monitor	
Data Recorder	

The *Input variables* tool loads some initialisation parameters and the specification of the current *run*, i.e. data taking session. Three types of run are available: a test run for PMTs calibration with LED, a pedestal run, and a beam run. The choice of one of these modalities influences the behaviour of the digitisers. For instance, a beam run is triggered by the BNB RWM (see section 5.2), while a test run is triggered by the LED pulser. The *PostSQL* tool updates an SQL database, where all the information about the run, such as the number of events and the start and the stop time, are saved. The *Trigger* tool blocks the Chain, awaiting and sending a trigger query to the VME. When the VME replies, the Chain is run back again. The *Network receive data* tool handles the data transfer via ZeroMQ messaging[2] between the main chain and the VME one. Real-time monitoring is provided by the *Monitor* tool, which also allows remote control of the DAQ.

On the VME side, the Chain communicates with the VME CPU retrieving all the information about the cards and the trigger. The *Trigger Sender* tool checks the status of the VME controller. If the ADCs are triggered, a trigger message is sent to the Main Chain. The data are dumped from the FPGA's buffer by the *Board Reader* tool and are sent to the Main Chain via ZeroMQ messaging over TCP protocol, thanks to the *Network send data* tool. The last tool of the Main Chain, *Data recorder*, saves data into a ROOT tree structure, where each entry corresponds to a full buffer of an ADC card (four channels). The buffer is is 160 000 samples long, and is split by a post-processor

[2] *ZeroMQ* is a high-performance asynchronous messaging library, aimed at use in distributed applications. The API provides *sockets*, each of which can represent a many-to-many connection between endpoints, operating with a message-wise granularity. ZeroMQ is developed by a large community of contributors and distributed under the LGPL license [40].

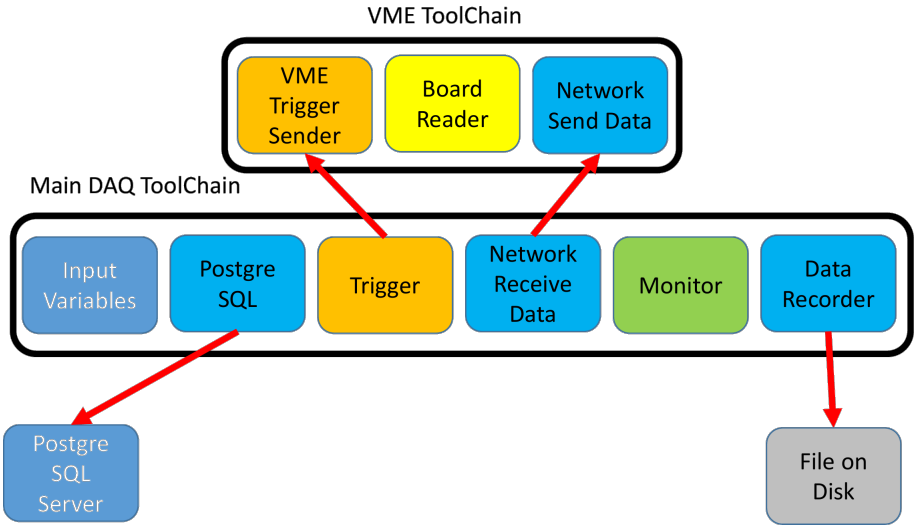

Figure 3.2: ANNIE's current main DAQ makes use of two parallel tool chains. All communication is provided by ZeroMQ messaging [40].

into sixteen digitised time profile, so four per channel, given by consecutive 80 μs data sets (10 000 samples long). The baseline is calculated and subtracted from the time profiles, and the precise time stamp is reconstructed; moreover, each channel is mapped to its equivalent PMT. An example of time profile is shown before and after the post-processing in Fig. 4.1. This passage reduces the file sizes by nearly a factor of four. Provided that the spill's frequency is $\sim$15 Hz and four spills are acquired, the buffer takes around a quarter of a second to fill. The slowest steps of the chain are readout and data transfer, which is temporary supported by RAM memory. The transition is meant to happen between pulse trains, so as to minimise the number of spills lost. Disk saving is threaded, therefore it does not impede data acquisition. A whole execution of the chain lasts nearly a second, slightly less than the pulse train frequency.

3.2 MRD Chain

3.2.1 Hardware

As explained in section 3.1.2, the signal from the veto and two layers of the MRD are logically summed and read by the VME digitisers. The PMTs of these two detectors are supposed to be read individually by both time-to-digital Converters (TDC) and ADCs in future stages of the experiment, and for this purpose a third ToolChain has been developed to collect data from both detectors. Two CAMAC[3] electronic modules are employed for these two detectors: LeCroy 3377 modules for the time digitisation, while LeCroy 4300B for analog conversion.

The LeCroy Model 3377 is a 32-channel TDC and optimised with a low conversion time and a high speed readout of 100 ns/word. The longest time window achievable is 4 088.0 ns, using a resolution of 4.0 ns, with 10-bit words. A delayed signal from the RWM acts as a "common start" for the TDC cards and each internal counter is stopped

[3] *Computer-Aided Measurement And Control* (CAMAC) is a bus and modular-crate electronic standard for data acquisition and control used mainly in nuclear and particle physics experiments and in industry. The bus allows data exchange between plug-in modules and a crate controller, which then interfaces to a CPU or to a VME-CAMAC interface.

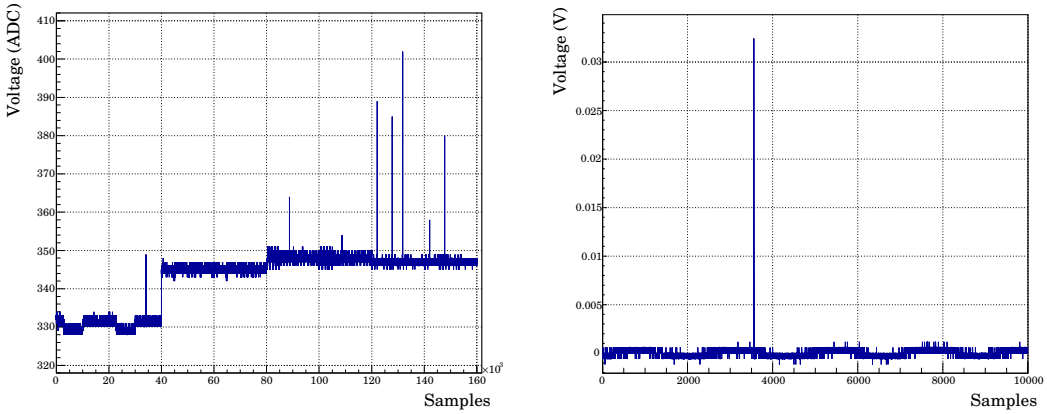

(a) The full buffer retrieved from a single card is 16 000 samples long. The voltage offset is different for each channel. The whole profile is split between the four channels, which in turn contain four consecutive acquisition of the beam spill.

(b) This is a single spill acquisition, trimmed by the post-processor from the full buffer. The baseline is restored.

Figure 3.3: Time profile before (**a**) and after (**b**) the post-processing.

by individual hit signals. The channels are fed with the discriminated PMT signals from the veto and the MRD.

The LeCroy Model 4300B FERA contains 16 independent 11 bit charge-to-digital converters. An 8 bit register and a memory containing the individual pedestal values to be subtracted from each ADC are also available. These converters haven't been installed in the electronic chain yet. However the software interface has been developed anyway.

All the cards are addressed via the Weiner CCUSB controller module. The CCUSB is a full-featured CAMAC Crate controller with integrated high speed USB 2.0 interface. For fast data acquisition applications the CCUSB has a built-in command list sequencer, called *command stack* with data buffering in a 22 kB size FIFO. A XILINX Spartan 3 family FPGA performs all CCUSB logic and functions.

3.2.2 Software

The work of this thesis work is mainly focused on the development of a dedicated data acquisition system for the CAMAC electronics of the experiment. A separate MRD DAQ has been created from scratch within the ToolDAQ Framework and with the help of some dedicated C++ classes, in order to properly acquire the veto and the MRD data. The CCUSB vendor provides a low-level C++ class to interface the controller with a computer. This was implemented in high-level C++ classes, which were developed with the purpose of handling the modules more easily. A base class takes care of opening the USB connection for the CCUSB controller and storing information on the cards, such as the Slot number; it also allows the configuration of the command stack. Two derived classes implement wrapper functions to deliver CAMAC commands via the NAF addressing[4].

[4]NAF module addressing is achieved knowing the slot Number, the sub-Address, and the Function code. Every CAMAC its own addresses.

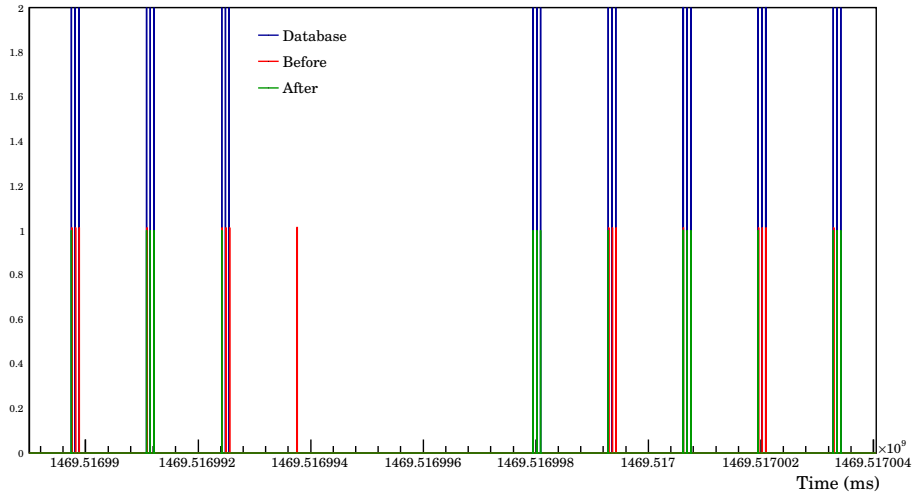

Figure 3.4: Detail of the time stamp alignment with the database data. The measured timestamps (red) are synchronised with the FNAL database (blue); thus, these get correctly overlapped by the definitive timestamps (green) after the post-processing. The synchronisation algorithm relies on pattern identification of the spills.

The MRD's ToolChain employs the CAMAC classes to interface with the controller and the cards. The Tools contained in the Chain are:

MRD
Trigger
LeCroy
Root output

The *Trigger* tool reads the FIFO of a specified card: if it is not empty, then all cards presenting data are read and the other tools are executed. Currently, a hit signal is generated in each TDCs by delaying the common start signal of ~ 1 μs, such that the FIFOs are never empty in coincidence with the beam's spills. Three triggering behaviours are supported: external trigger, software trigger with random card access, and software trigger with card test function. The *LeCroy* tool is meant to work for both the TDCs and ADCs cards: if only either TDCs or ADCs are employed, then just one tool must be daisy-chained; otherwise, if both are used, then two tools are required. The last tool fills a ROOT tree, containing the acquired data and their timestamps, i.e. UNIX time retrieved from an NTP server, which uses GPS time sources. The time of each event is fundamental because it allows the correlation between the Main DAQ and the MRD DAQ, which run as a standalone process on a different computer.

As a matter of fact, a time drift in the MRD timestamps has been found, likely due to imprecise synchronisation with the NTP server which occurs every 1024 ms and is accurate to less than 30 ms. For this reason, a post-processor was realised to fix the timestamps correlate the events between the two DAQs. In this way the events from the two DAQs can be related to each other, with the help of the FNAL spill database. A detail of the result of the synchronisation is plotted, in Fig. 3.4. This method is effective as long as the frequency of the chain execution is greater than the spill frequency, which is 15 Hz, so as not to miss any beam event. However the CAMAC event rate is

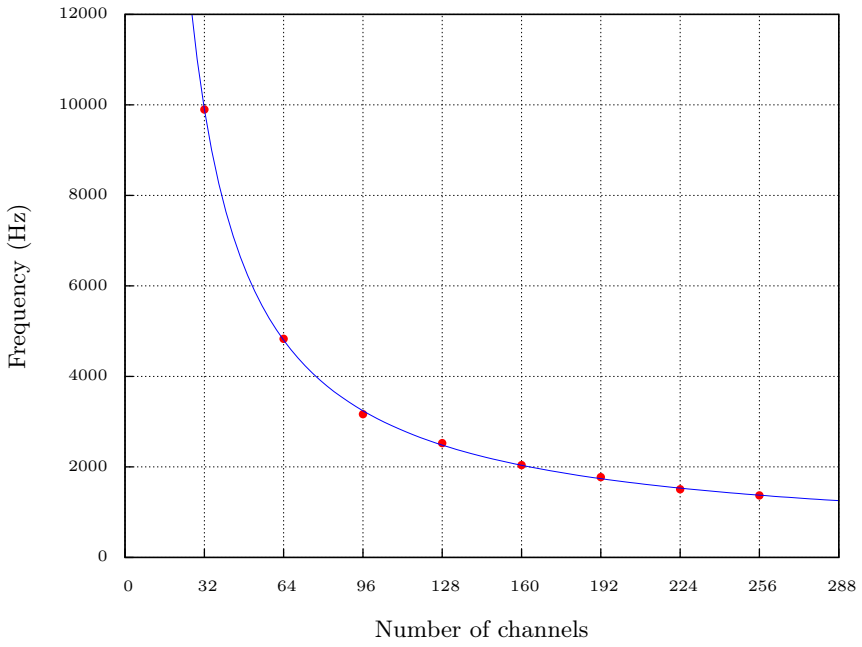

Figure 3.5: The frequency of the DAQ in reading TDCs with all channels fired, but 1.3% time occupancy The behaviour is $1/x$, meaning that the reading bandwidth per channel is fixed.

quite low in this early stage of the experiment, around 0.20 Hz[5]. This suggest that the modules present data effectively only the ∼1.3% of the time. The longest portion of the MRD DAQ is the CAMAC addressing and data collecting. The software is tested using software triggering, employing the test functions of the modules, and counting the time required for 100 000 repeated cycles with 1.3% firing probability; the frequency was afterwards estimated. The result is shown in Fig. 3.5, where frequency vs number of channel is plotted for TDC modules. It's clear that the frequency is well above the lower theoretical limit of 15 Hz. Rescaling the frequency to full time firing, i.e. the number of channel to be read is maximum for every DAQ cycle, the limit is easily reached with just ten modules, corresponding to five layers of MRD, Veto excluded.

3.3 Future improvement

3.3.1 Zero-suppression

As of now, the DAQ acquires 80 μs time windows in their entirety. This implies that also unimportant data are collected. In fact, the majority of every time window is mostly electronic noise, whereas the meaningful information is limited compared to the length of the time window. This leads to unnecessary memory occupancy. An *online zero-suppression* method is planned to be implemented for the next phases of the experiment, in order to definitely overcome storage needs. The preliminary data analysis supports this decision, as explained in section 4.4.

[5]The rate is measured from output ROOT file, dividing the number of entries, i.e. events, by the time passed between the first and the last timestamp.

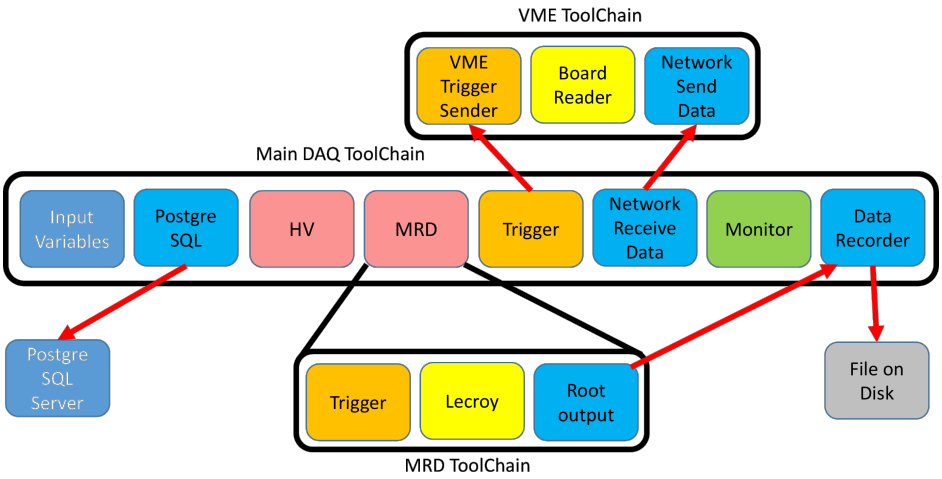

Figure 3.6: A possible final version of ANNIE's DAQ, with all the Chains integrated. The MRD ToolChain could be implemented as a Tool of the Main Chain, thanks to the scalability of the software.

3.3.2 DAQ integration

The final version of the DAQ system needs a full integration of the Main Chain with the CAMAC one. A possible solution is depicted in Fig. 3.6. A new tool could be employed to embody a simplified version of the MRD ToolChain, rather than run it in a parallel process. The MRD Chain is fast in execution, as proved in the previous section, so it should not significantly slow down the Main DAQ. In this way, the TimeStamp synchronisation technique is not required anymore because all the acquisitions are done by the same CPU and simultaneously. The output files could be merged into a single one by synchronising the two recording tools with ZeroMQ communication. Final reconstruction of PMTs data and MRDs could be done in a single post-processing stage.

Chapter 4

Data Analysis procedures

Interpreting electronic signals produced by the detector is a mandatory step for event reconstruction. Energies, momenta, and directions of the involved particles must be estimated in order to determine the detected physical interaction, the study of which is the ultimate goal of the experiment. ANNIE's early stage data have been studied with analysis algorithms which were developed and tested from scratch: they are implemented in a purpose-built software, which studies the signals acquired from the water PMTs. The code's procedures relies on individual pulse analysis and is largely focuses on the rejection of background with respect to signals. Some of the methods illustrated in this chapter could be employed into a more complete analysis framework, valid even for future phases of the experiment. The plots reported here were realised using the Neutron run data, unless otherwise stated.

4.1 Data selection

The Main DAQ is programmed to create a new *Run* every time the Chain is stopped and restarted. Being an R&D phase, the DAQ has been stop-and-started many times during data taking, because different configurations of the experiment were set up and tested in various occasions. The size and the number of post-processed files, that constitute the runs, are therefore not constant, despite high statistics were achieved most of the time. The post-processed ROOT files (see section 3.1) from the DAQ are used in the data analysis. The buffer retrieved from the VME boards is properly split for each trigger, either hardware or software, in that each set of data consists of 80 μs worth of digitised signal. A single file holds 383 full buffers and this translates to 1532 triggers, which corresponds to 122.560 ms. Two distinctive runs were selected as model data sets, with the intention to outline the best data analysis procedures:

Cosmic: run with a random trigger, therefore out of sync with the beam: the signals in this set are mostly given by cosmic muons;

Beam: run in sync with the beam, and with a 8″PMT mounted on top of the NCV, in order to observe neutron captures.

Their quantitative features are shown in Tab. 4.1.

4.2 Individual pulse analysis

The analysis software scans all the post-processed time profile which constitutes the run, as the one shown in Fig. a of 4.1, sorted by trigger and PMT number. Any peak

Table 4.1: Runs selected for data analysis. They are composed of different numbers of file, resulting in diverse number of triggers. Total time is the number of triggers times 80 μs. The listed memory sizes refer to the post-processed files.

Run type	**N of files**	**N of Triggers**	**Total time** (ms)	**Data size** (MB)
Cosmic	142	217 544	17.4×10^3	106.1×10^3
Beam	164	251 248	20.1×10^3	122.5×10^3

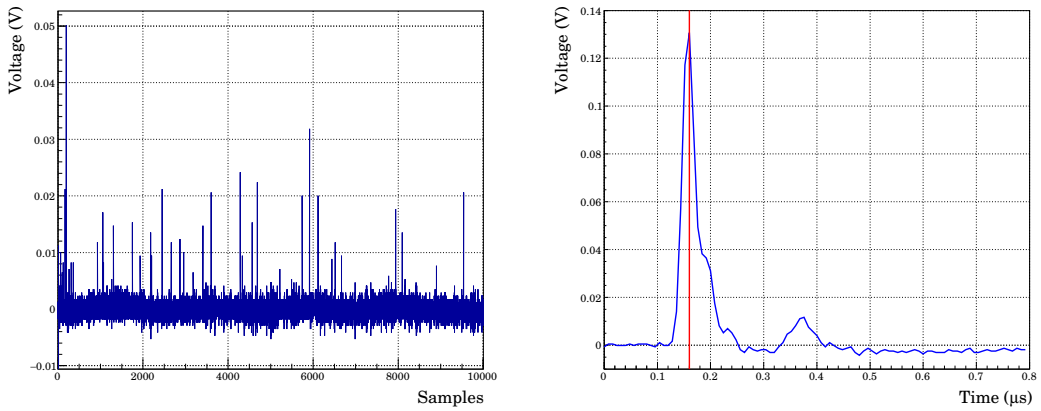

(a) Time profile of a single trigger, where all the pulses of the sixty PMTs are overlaid and are trimmed yet.

(b) Time profile of a single pulse. The red line marks the 20 % of the window's length, at 0.16 μs. Two main peaks are visible in this pulse, about forty nanoseconds apart: it is the time that light takes to travel back and forth inside the tank (see section 2.1).

Figure 4.1

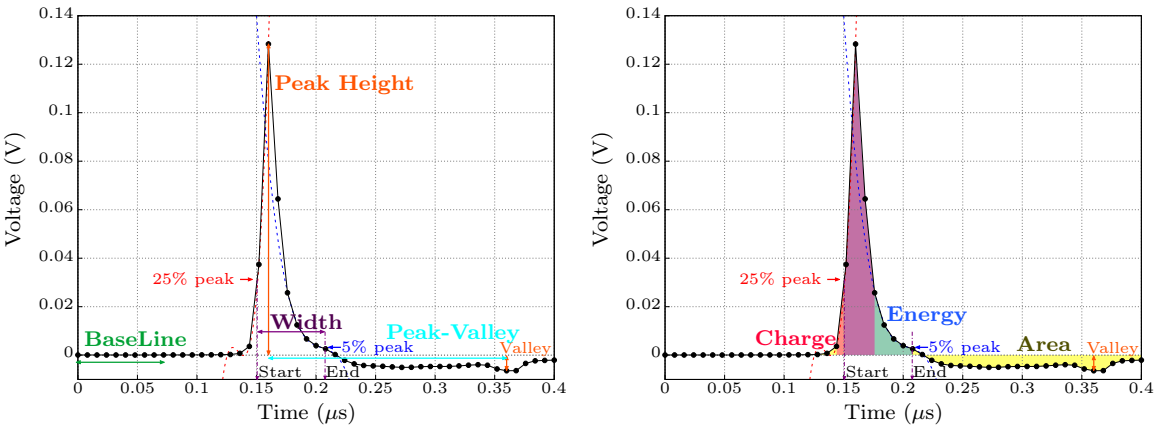

(a) From left to right: in green the *Baseline*, in orange the *Peak* height, in purple the *Width*, and in light blue the *Peak to Valley* time distance.

(b) From left to right: in pink the *Charge*, in blue the *Energy*, and in gold the *Area*. These three integrals cross over each other in the purple region.

Figure 4.2: Illustration of the pulse analysis values. The *25 % peak height* marks, which define the *Start* and *End* of the signal, are common to both diagrams. The dashed lines represent the cubic interpolations. The shape was realised averaging the collected pulses.

above a certain voltage threshold, V_T, is selected and an enclosing time window of a predefined length, L, is trimmed around it. A length of $L = 100$ samples is chosen, resulting in a 0.8 μs long window. The position of the peak inside this window is set to 20% of its length, i.e. the peak is always set at 0.16 μs from the beginning of the time window. These subsets of data are called *pulses* and are collected in a separate ROOT file. The choice of window length and the peak position is the result of a compromise between execution of the code, memory usage and loss of physical information. Many pulses show consecutive multiple peaks, as the one in Fig. b of 4.1, mainly because of light reflections in the water tank. A shorter time window might not include secondary peaks, significant for proper energy evaluation.

Each pulse is individually analysed and processed. As a result, a set of parameters which characterise the pulse is computed, in addition to Veto and MRD coincidences. The following analysis relies on these quantities, graphically outlined in Fig. 4.2, which are labelled as follows:

Baseline: arithmetic mean of first ten points of the pulse; this value is then subtracted from the whole array;

Peak: height of the peak (maximum) with respect to the zero;

Start: position in time of the 25% of the rising edge of the pulse, estimated with precision using cubic interpolation;

Previous: time difference between the Start of the pulse and the Start of the previous pulse, if from the same PMT.

Peak to valley: time distance from the peak to the valley (minimum), related to the falling edge duration;

Width: time that spans from Start to the 5% of the falling edge of the pulse (End), calculated using the same algorithm employed for Time;

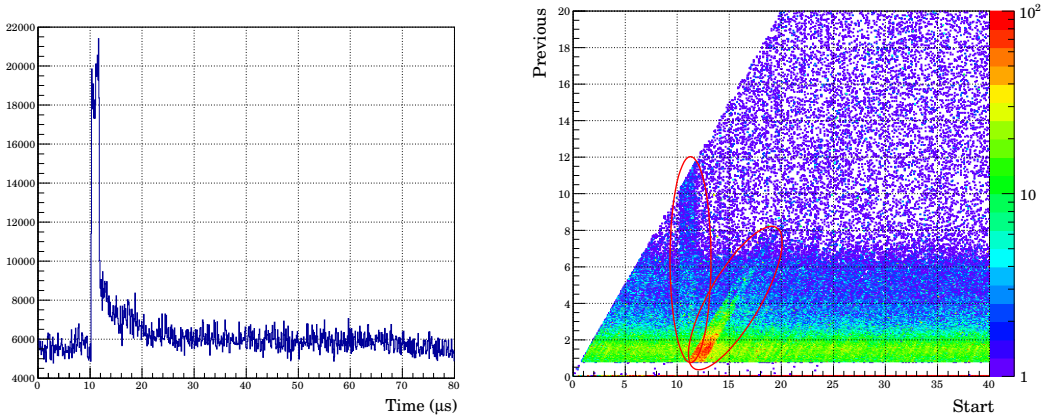

(a) *Start* spectrum of a beam run. The count concentration with respect to the background suggests that the beam occurs ten microseconds after the beginning of the data acquisition. The second half of the 80 μs buffer is basically free of beam related pulses.

(b) *Start* is plotted against *Previous*; both axes are in μs. The beam pulses are split into two groups: the correlated pulses (slanted ellipse) are beam related events, while the uncorrelated pulses (vertical ellipse) are likely due to afterpulsing.

Figure 4.3: Time distribution of the pulses of a beam run.

Charge: sum of the 5 points around peak, weighted with the bin width;

Energy: integral of the signal form the Start to the End;

Area: area of the absolute value of the pulse;

Time of flight: time difference between the Start and RWM signal;

Since ANNIE is a water Cherenkov detector, the event reconstruction relies on time and energy evaluation of the signals, and for this fact these two quantities must be measured precisely. First of all, each pulse is shifted such that the first ten points of the shape have null mean. Doing so, the *Baselines* are normalised and the peaks of the signals become comparable. The *Starts* are determined with high precision thanks to data interpolation[1], within the time resolution of the ADCs. An example of their spectrum is plotted in Fig. a of 4.3. A very relevant variable is in general the time delay between consecutive pulses, because it gives a handle on systematic errors. This fact is emphasised in particular in ANNIE, where neutron detection is the main goal. In fact the distinctive feature of neutron capture by gadolinium is a delayed signal, detectable tens of microseconds after the main interaction. The *Previous* entry has the potential to accommodate this necessity and reveal other interesting features. For instance, Fig. b of 4.3 shows that the consecutive pulses related to the beam are correlated in two ways.

Two interesting and similar quantities are the *Peak to Valley* and the *Width*, the spectra of which are reported in Fig. 4.4. The minima, or valleys, are given by negative peaks, which are also visible in averaged pulses. They could be likely due to electrical reflection, caused by an impedance mismatch between cables and front-end electronics: a smaller impedance on the propagation line leads to a reflection with the same sign; the signal is sent back again and inverted when it meets the high impedance of the PMTs. Overall, the reflection covers the length of the line twice. The *Peak to Valley* spectrum

[1]The algorithm looks for four points around the threshold (25 % for the *Start* or 5 % for the *End*), which are used to define a cubic function. Using Newton's method, the correct time position is found.

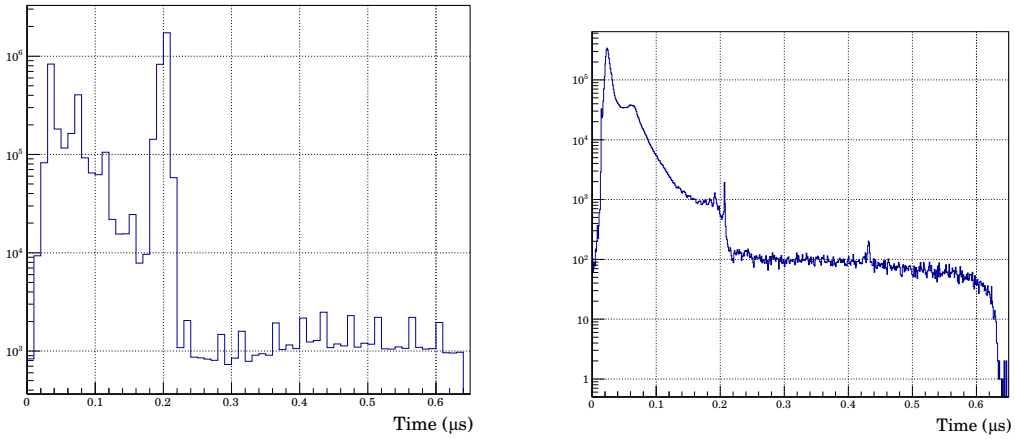

(a) The distance of the valley from the peak in time. The mode of the spectrum is at 0.2 μs.

(b) Distribution of *Width* in logarithmic scale. The spectrum presents an edge near two hundred nanoseconds and then becomes flat. Another edge is visible, close to the peak at shorter widths.

Figure 4.4: Spectra of *Peak to Valley* and *Width*. In both cases, the plot utterly changes for time intervals larger than two hundred nanoseconds.

suggests that the time delay of the reflection is near 0.2 μs, which is consistent with the time needed for a PMT signal to travel to the digitisers, a hundred nanoseconds.

Estimating the energy of each shape is more complicated, because of multiple reflections and afterpulsing signals. An evaluation of the pulse integral would be a good indicator of the total charge deposited on each PMT. Three different methods to estimate the area enclosed in a pulse have been implemented. *Charge*, *Energy*, and *Area* are all approximations of the charge released by an incoming photon. As shown in Fig. b of 4.2, there is a partial superimposition of the three: they show indeed interesting correlation patterns, reported in Fig. 4.5. The *Energy* is employed for following analysis, as it best fits the pulse's area.

The time distribution of the peaks is studied for each trigger, as well as the time coincidences between the PMTs signals. Pulses are considered simultaneous when they are less than 0.8 μs apart. In this way, signals close to each other are grouped together. The number of the coincidences in the cluster easily translates to the number of PMTs fired at the same time, N_{PMT}; when the latter exceeds a defined threshold, all the simultaneous pulses are tagged as *event*, the time position of which is afterwards calculated by a weighted average of the adjacent signals, i.e. the centroid of the cluster. The nature of the detected interaction may be established reasonably well from the number of pulses of the event. For instance, a cosmic muon coming from above would project the Cherenkov radiation on the bottom of the tank, thus illuminating the majority of the water PMTs. On the other hand, a muon from the interaction of a beam neutrino with a nucleon would emit photons along the beam direction, but only a portion of the light cone could be captured, and the PMTs would result less active. Even natural radioactivity, caused by radionuclides in the glass of the phototubes, can be detected, although these events have only few coincidences and are readily filtered by a proper threshold of N_{PMT}. A rich event cluster is shown in Fig. 4.6. Not every pulse in the trigger belongs to an event. For instance, in Fig. 4.6 there are at least four pulses outside from the main pulse cluster. These might be generated by background sources and therefore they should not

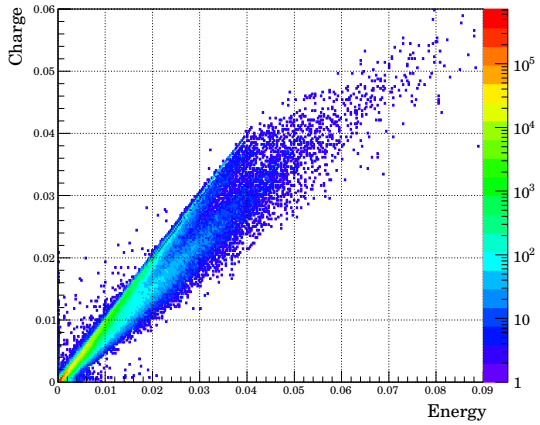

(a) The *Charge* (V·μs) is plotted against the *Energy* (V·μs).

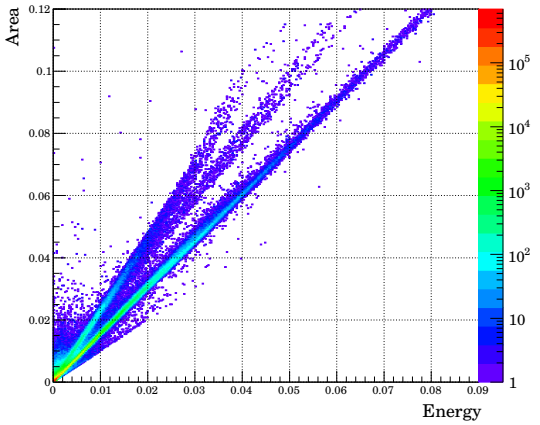

(b) The *Area* (V·μs) is plotted against the *Energy* (V·μs).

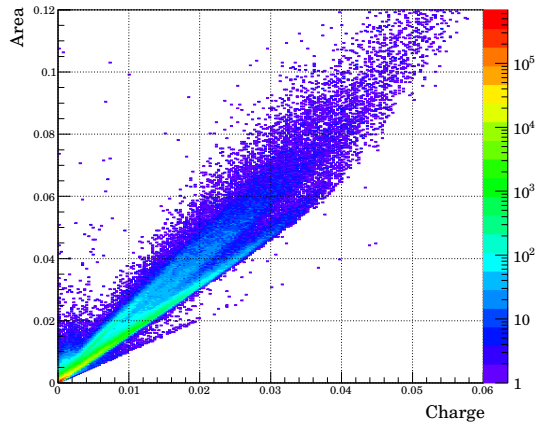

(c) The *Area* (V·μs) is plotted against the *Charge* (V·μs).

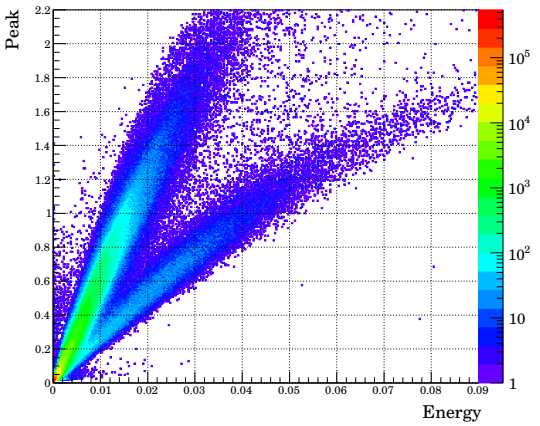

(d) The *Peak* (V) is plotted against the *Energy* (V·μs).

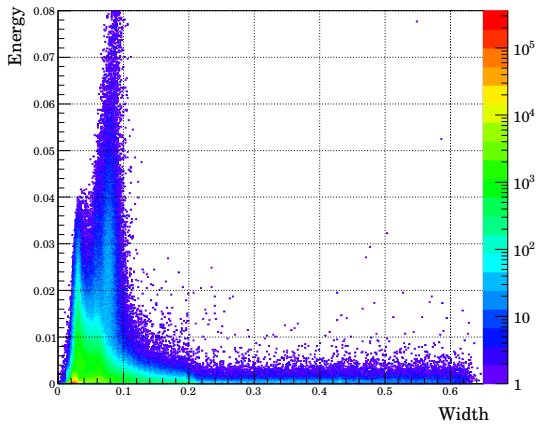

(e) The *Energy* (V μs) is plotted against the *Width* (μs).

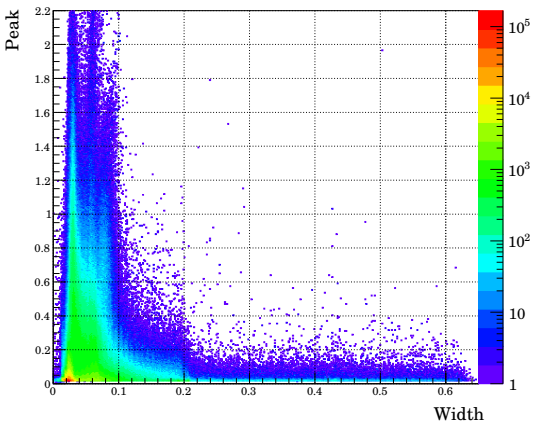

(f) The *Peak* (V) is plotted against the *Width* (μs).

Figure 4.5: Correlation plots of the three integral quantities. Two or more linear correlations with different coefficients are visible in the plots **a**, **b**, and **c**, which suggests that there is a variety of pulse widths. This effect is emphasised in the plot **d** where the separation between the tails is pronounced: pulses with the same peak height may have very distinct energies, and vice versa. The width spectrum, as in Fig. b of 4.4, is stretched in plots **e** and **f**, and two or more widths appear.

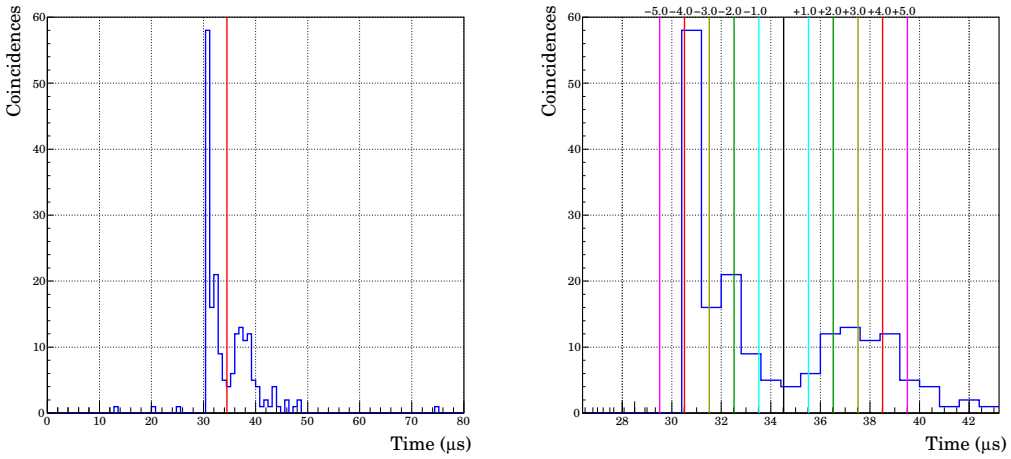

(a) The red line marks the weighted average of the coincidences, which is 34.51 μs in this example.

(b) The coloured lines mark the five time window for background rejection, Δ_T in μs, listed in Tab. 4.2.

Figure 4.6: Both plots show the same histogram, which is filled with the *Start* time of each pulse belonging to the same trigger. A cluster of pulses is found from 31 μs onward: it is an event. In this particular case, the time span of the event is considerably long, in that the PMTs are producing pulses for about twenty microseconds.

be included in the event reconstruction. In order to discriminate the pulses, an arbitrary time interval of radius Δ_T is defined around the event time position. A pulse that falls within this window is designated as *signal*, otherwise as *background*.

4.3 Signal discrimination from background

Being a first stage study, the algorithm only relies on V_T, N_{PMT}, and Δ_T, in order to distinguish signal pulses from background ones. Even for future analysis framework, it is necessary to determine the best combination of the three parameters; so, these have been varied and data analysed multiple times. Twelve combinations, which are listed in Tab. 4.2, were chosen. The variation of the voltage threshold affects the total number of pulses, because any peak below V_T is neglected. The five values employed are all well above the electronic noise, which is order 1 mV.

The ratio between signal and background is governed by the other two parameters, namely the number of PMTs fired and the rejection time window. Respectively four and five values were picked for these parameters. The increase of N_{PMT} restricts the number of signals, as suggested by Fig. 4.7 where the the number of event coincidences, i.e. the number of PMTs fired simultaneously, is plotted. The peak close to $N_{\mathrm{PMT}} = 58$ is likely due to high-multiplicity cosmic muon events. The time allowance of the event was also studied, varying the Δ_T parameter. Understanding the relevance of belated photons, possibly given by reflection inside the tank, is decisive for developing a correct analysis framework. The selected intervals are illustrated in Fig. b of 4.6.

The data sets show different number of pulses and a different balance between signals and backgrounds. The processed data sets present therefore different number of pulses and different proportion between signals and backgrounds. These quantities are summarised in Tab. 4.3. The effects of the different combination of the analysis parameters

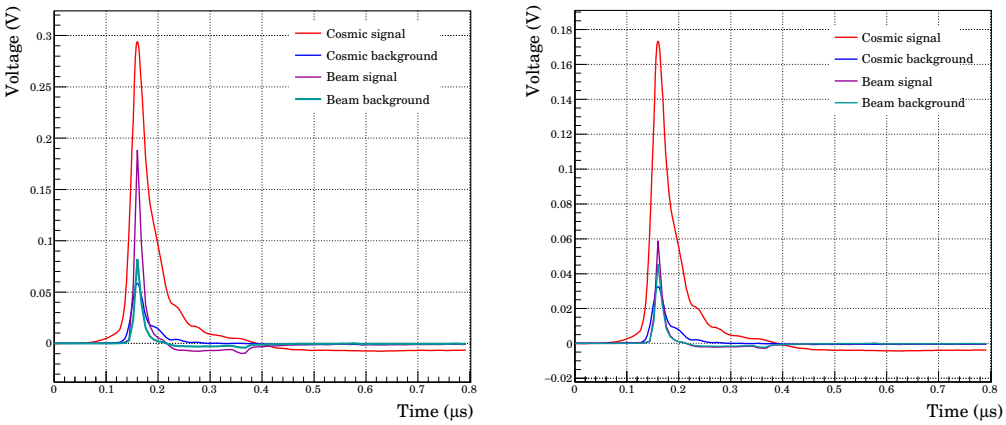

(a) C

(b) V_{00}

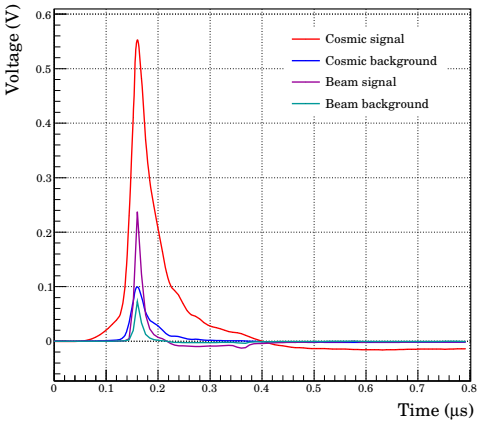

(c) N_{50}

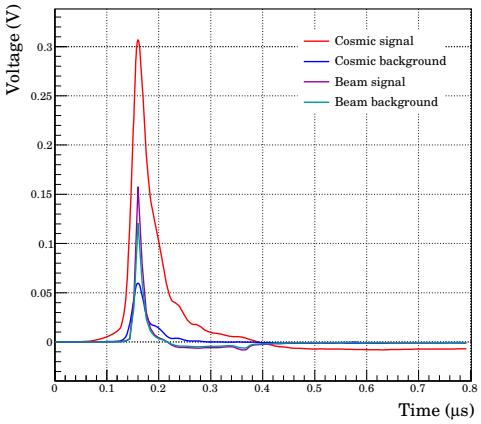

(d) Δ_{10}

Figure 4.8: Average pulse for Cosmic and Beam's signals and backgrounds from four different data sets: C, V_{00}, N_{50}, Δ_{10}. The shapes are all similar, even though their size changes. The proportion between peak heights imply that the Beam data are more influenced by the variation of the parameters.

Table 4.2: The combination of the employed thresholds. The first one, in bold letters, has parameters common to every subset.

Label	V_T (V)	N_{PMT}	Δ_T (μs)
C	0.02	10	4.0
V_{00}	0.005	10	4.0
V_{01}	0.01	10	4.0
V_{05}	0.05	10	4.0
V_{10}	0.10	10	4.0
N_{15}	0.02	15	4.0
N_{30}	0.02	30	4.0
N_{50}	0.02	50	4.0
Δ_{50}	0.02	10	5.0
Δ_{30}	0.02	10	3.0
Δ_{20}	0.02	10	2.0
Δ_{10}	0.02	10	1.0

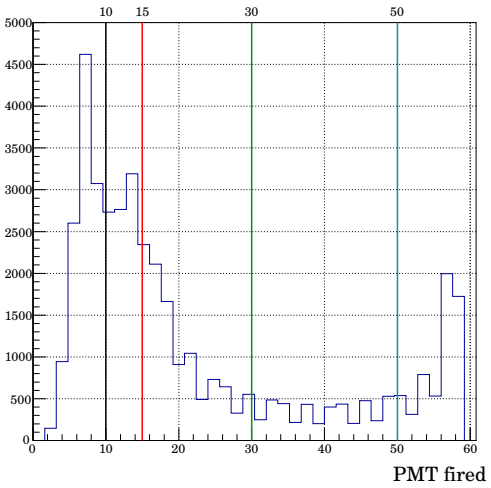

Figure 4.7: Frequency of the number of PMTs hit in an event. The coloured lines mark the four N_{PMT} values listed in Tab. 4.2.

can be also appreciated by looking at the average shape. In Fig. 4.8, four data sets are selected, as an example, and the plot is shown for both the cosmic and the beam run. The shape of the pulses basically doesn't change, but the size and the proportion between signals and backgrounds do; thus, they are sensitive to the three parameters, V_T, N_{PMT}, and Δ_T. The other eight data sets present similar variations.

4.4 Data size reduction

A zero-suppression method is planned to be implemented in the data acquisition system for the next stages of ANNIE. As a matter of fact, most of the digitised time window from the VME cards is of no use for event reconstruction (see the Time column in Tab. 4.3). Taking advantage of circular memory, this technique basically selects and records a narrower buffer every time an arbitrary voltage threshold is reached.

In a similar way, the developed pulse analysis adopts an off-line zero-suppression method. It is easy to appreciate the benefits derived from this technique, just by looking at Tab. 4.4. The memory size of the analysed files is reduced by a factor between 30 and 300, with minima of the order of 1 000, depending on the choice of the parameters. The results indicate that V_T has the strongest influence on the final data size, as expected. The other two parameters, instead, are not of great concern, since they don't impact on the effective number of pulses. Combined with the post-processor software, which reduces the raw data files to almost a quarter of the initial size, the zero-suppression method could achieve a compression factor of about four-hundred, on average.

Table 4.3: Number of pulses in the Cosmic and Beam run. The Signal column is the ratio between the number of signals and the total number of pulses; the Time column is the ratio between the total time of the pulses, which is their number times 0.8 μs, and the total time of the run, from Tab. 4.1; Signal to Background Ratio (SBR) is the ratio between signals and backgrounds.

	Cosmic				Beam			
Label	Total	Time (%)	Signal (%)	SBR	Total	Time (%)	Signal (%)	SBR
C	1 869 473	8.6	21.2	0.269	5 023 868	20.0	46.5	0.871
V_{00}	3 991 618	18.3	18.0	0.220	16 459 218	65.5	25.3	0.338
V_{01}	3 199 707	14.7	17.7	0.214	12 203 561	48.6	29.3	0.415
V_{05}	546 497	2.5	46.2	0.858	2 128 895	8.5	69.3	2.261
V_{10}	342 258	1.6	58.5	1.408	1 391 752	5.5	77.6	3.461
N_{15}	1 865 579	8.6	19.3	0.240	4 881 223	19.4	54.2	1.182
N_{30}	1 859 539	8.5	16.4	0.197	4 743 670	18.9	41.5	0.746
N_{50}	1 850 590	8.5	1.6	0.016	4 616 384	18.4	34.3	0.521
Δ_{50}	1 869 473	8.6	21.3	0.270	5 023 868	20.0	49.2	0.967
Δ_{30}	1 869 473	8.6	21.1	0.267	5 023 868	20.0	43.7	0.778
Δ_{20}	1 869 473	8.6	20.8	0.263	5 023 868	20.0	36.2	0.568
Δ_{10}	1 869 473	8.6	19.7	0.246	5 023 868	20.0	29.1	0.410

Table 4.4: Data sizes of the analysed data sets. The *ratio* columns present the ratio between the final data size and the original size of the post-processed files, listed in Tab. 4.1.

	Cosmic		**Beam**	
Label	Data size (MB)	Ratio %	Data size (MB)	Ratio %
C	329.331	0.310	675.355	0.886
V_{00}	621.029	0.585	1 779.345	2.333
V_{01}	510.056	0.481	1 384.335	1.815
V_{05}	121.439	0.114	351.355	0.461
V_{10}	91.656	0.086	249.068	0.327
N_{15}	326.970	0.308	669.110	0.877
N_{30}	321.029	0.302	646.297	0.848
N_{50}	318.970	0.301	631.707	0.828
Δ_{50}	320.291	0.302	678.463	0.890
Δ_{30}	321.040	0.302	675.090	0.885
Δ_{20}	321.896	0.303	679.243	0.891
Δ_{10}	320.299	0.302	666.223	0.874

Chapter 5

Data analysis results

Analysis results are presented in this chapter and, where possible, compared with simulation. The plots reported here were realised using the C data set, unless otherwise stated.

5.1 Results with the Cosmic run

5.1.1 Cosmic muons

With the beam off, only cosmic rays leave a trace in the ANNIE detector. According to Eq. 1.37, the energy threshold for muons is $E \gtrsim 160$ MeV, with $n = 1.33$, given that the muon mass is 105 MeV[1]. The average energy of the muon reaching the ground is well above the Cherenkov threshold, so the nominal flux at sea level can be used to evaluate the cosmic background rate. The water tank is placed eight meters below the surface, and it fits the hall's walls, hence only the top area of the tank (slightly more than 7 m^2) could be taken in consideration. A rough estimation suggests that the rate of muons reaching the detector is

$$I \simeq (7\, I_0)\ \mathrm{m}^2 \simeq 1\,036\ \mathrm{Hz}\,. \tag{5.1}$$

where I_0 read from Eq. B.4. This rate can be estimated, counting the events found by the analysis algorithm. For a more realistic estimate, events that show coincidences with the Veto or the MRD are discarded. The Beam run could also be used for this evaluation, for instance exploiting the fact that beam events are limited to the first half of the 80 μs buffer. However either the Veto or the MRD are active most of the time, being the trigger synchronised with the beam, therefore the tally is not feasible, but with the Cosmic run. The rate is therefore given by the ratio between the number of events and the total time taken in consideration. The number of pulses in this kind of event are also counted in order to evaluate the average number of pulses in a muon event. The measured rate is found to be, on average, half of the predicted value in Eq. 5.1. This difference is brought about by a combination of the detector's efficiency (geometry and photodetector quantum efficiency) and the validity of the data analysis algorithm. The results are shown in Tab. 5.1. The Δ_T parameter doesn't influence the count of the cosmic muons as much as the other parameters do. The cut in the PMT number selects the most energetic events, while the voltage threshold removes low energy pulses, instead.

[1]The muon mass is known with an accuracy of order 10^{-8}. According to the PDG, $m_\mu = 105.658\,371\,5 \pm 0.000\,003\,5$ MeV.

Table 5.1: Cosmic muon rate, estimated using the analysed Cosmic run. The total time is given by the number of triggers time 80 μs and is used to calculate the rate. The last columns is the ratio between the measured rate with the theoretical one, in Eq. 5.1.

Label	Trigger	Signals	Pulse	Mean pulse	Rate (Hz)	Ratio (%)
C	217 530	8 078	330 111	40.9	464.2	44.8
V_{00}	225 412	14 210	635 602	44.7	788.0	76.1
V_{01}	222 539	11 362	488 371	43.0	638.2	61.6
V_{05}	111 640	5 590	229 456	41.0	625.9	60.4
V_{10}	59 690	5 056	195 273	38.6	1 058.8	102.2
N_{15}	216 157	6 692	296 674	44.3	387.0	37.4
N_{30}	214 474	4 980	247 709	49.7	290.2	28.0
N_{50}	210 007	458	25 212	55.0	27.2	2.6
Δ_{50}	217 506	8 079	331 452	41.0	464.3	44.8
Δ_{30}	217 574	8 095	328 772	40.6	465.0	44.9
Δ_{20}	217 634	8 122	324 632	40.0	466.5	45.0
Δ_{10}	217 964	8 135	307 014	37.7	466.5	45.0

Table 5.2: Fit result of the correlation of the plot max hit vs muon position. The function $y = \mathrm{a} + \mathrm{b}\,x$ was employed. The correlation is independent of the value of reflection.

Reflection	$\rho_{\mathrm{a,b}}$	a (cm)	b
0 %	−0.837	0.0 ± 0.2	1.001 ± 0.002
25 %	−0.866	0.2 ± 0.2	0.998 ± 0.002
50 %	−0.839	0.3 ± 0.2	0.998 ± 0.002
75 %	−0.862	0.0 ± 0.2	1.000 ± 0.002
87 %	−0.871	0.2 ± 0.2	0.998 ± 0.002
100 %	−0.878	0.1 ± 0.2	0.999 ± 0.002

5.1.2 Centre of interaction

Simple event reconstruction was undertaken with preliminary data, although the spatial resolution of the present photodetector array is limited. The idea is to analyse the pattern of the photon deposited on the PMTs, in order to infer the nature of the interaction which generated the Cherenkov radiation. As a first step, the Cosmic run has been taken in consideration, because it doesn't contain beam-related events, but muon ones; the validity of the selection method has been also tested, with also the help of an easy Monte Carlo simulation (see App. C).

For the sake of simplicity, the simulation generates only vertical muons, with $\beta = 1$, and the propagation of Cherenkov photons inside ANNIE's tank is reproduced. Muons don't enter vertically in the tank, but it can be considered as a strong assumption, taking into account the geometry of the hall of the experiment. The distribution of the photons on the bottom of the detector, with respect to the position of the entering muon and the reflection of the PVC liner, is thus studied. Five significant reflection percentages of the inner walls were chosen (0 %, 25 %, 50 %, 75 %, 100 %), in addition to the value given by the vendor (87 %). The amount of photons reaching the bottom of the cylinder is shown in Fig. 5.1, for each reflection values. This plot can help in pattern reconstruction of collected data, in which the role of the walls has not been determined yet.

The simulation also shows that the position of the muon is strongly correlated with

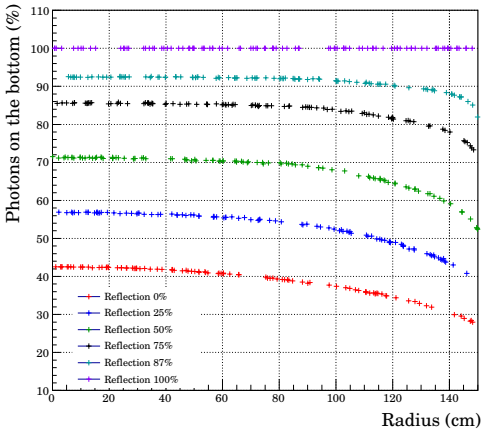

(a) As expected, all photons reach the bottom when the reflection is 100 %. If the walls fully absorb, about 40 % of the photons hit the base of the tank.

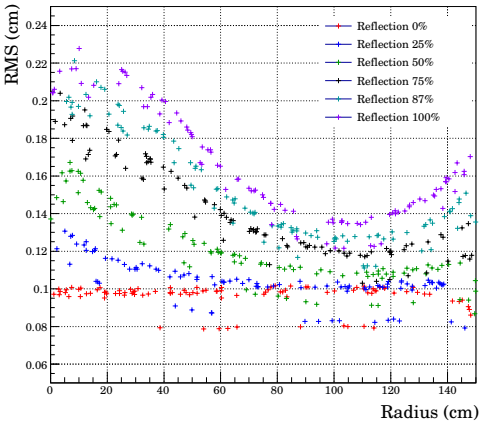

(b) Dispersion of the photon on the bottom of the tank. If the walls fully absorb, the photons are evenly distributed, otherwise the minimum dispersion is reached at about one metre from the centre.

Figure 5.1: Photons deposited on the bottom of the water tank, with different values of wall reflection. The x-axes is the distance of the muon with respect to the centre of the tank.

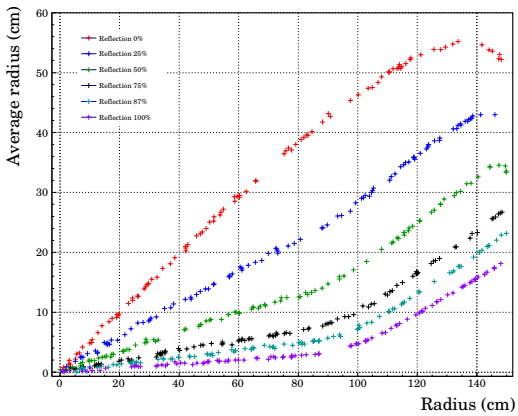

(a) Average distance of the deposited photons. The correlation is basically liner if the walls absorb all the light.

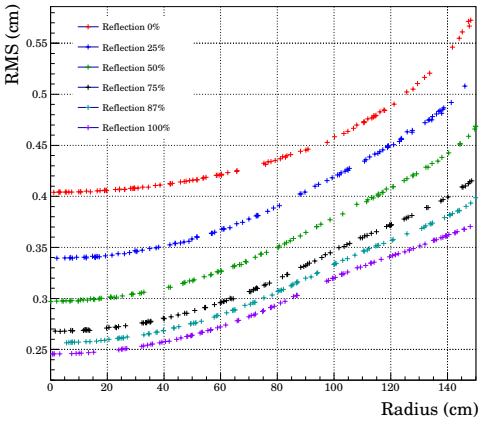

(b) Deviation of the distance of the deposited photons from the average. The relation is somehow parabolic within one metre from the centre of the tank. In all cases, the smallest dispersion occur for coaxial muons.

Figure 5.2: Correlation plots versus the distance of the muon with respect to the centre of the cylinder.

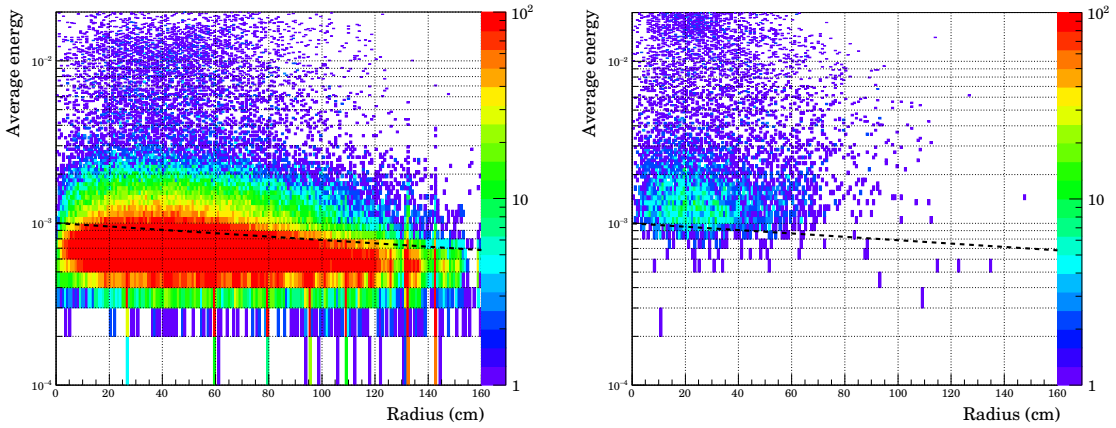

(a) Background data.

(b) Signal data.

Figure 5.3: Average energy distribution versus the barycentre of the PMTs, expressed as distance from the centre of the tank. The black dashed line is used to reject false positive events and corresponds to Eq. 5.2.

the spot of highest gathering of photons. A linear fit was computed and the results are listed in Tab. 5.2. This suggests that the position where most of the photons are deposited should be used when handling real data. On the other hand, the relation with the barycentre of the light pattern is less correlated and depends on the reflection of the walls, as shown in Fig. 5.2, even though the behaviour of the dispersion (RMS) of the photons is easier to interpret.

Regarding the collected data, space is discretised, because of the finite geometry of the photomultipliers. For this reason, using the position of the most frequently hit PMT does not provide any further information. The average position, $\hat{d}$, of the PMTs with respect to the centre of the water tank, weighted by the overall energy collected[2], is used, instead, and is plotted versus the average energy, $\hat{E}$, per pulse. In Fig. 5.3, the plot for both backgrounds and signals are shown. A far resemblance can be seen with the simulation results. An accumulation region is visible in the background plot, which is missing from the signal one. This area can be roughly separated with the following formula:

$$\hat{E} = 10^{-3} - 2 \times 10^{-6} \hat{d}\,. \tag{5.2}$$

The algorithm relies on time coincidences to select signals from backgrounds. For this reason, events with a wide dispersion, i.e. a high standard deviation, are more likely to deceive the selection method. Fig. b of 5.4 shows that backgrounds have a longer RMS distribution than signals. No meaningful correlation between the time RMS and the average energy has been found, as well as interesting patterns in the spectra, when applying the cut. The latter can however be used to count type I errors of the selection algorithm. The results are listed in Tab. 5.3. The efficiencies given by the voltage thresholds can be deceiving, in that the V_T data sets consider less and less pulses. The PMTs coincidences and the time rejection window have a slighter influence on the false positive count, but the trend is nevertheless clear.

[2]The definition of energy is conveyed in section 4.2.

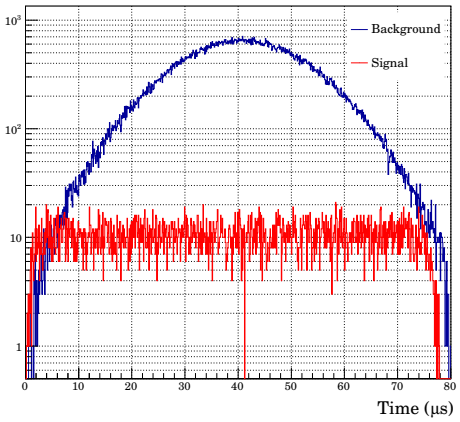

(a) Arithmetic mean of the arrival time. The backgrounds follows a perfect gaussian distribution, while the signals fit a uniform distribution.

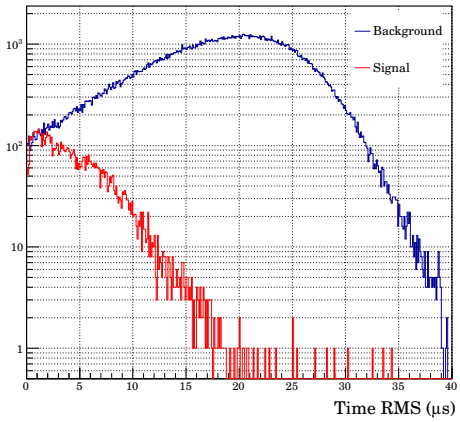

(b) Standard deviation of the arrival time.

Figure 5.4: These plots show the arithmetic mean and the dispersion of the time position of the pulses belonging to the same event.

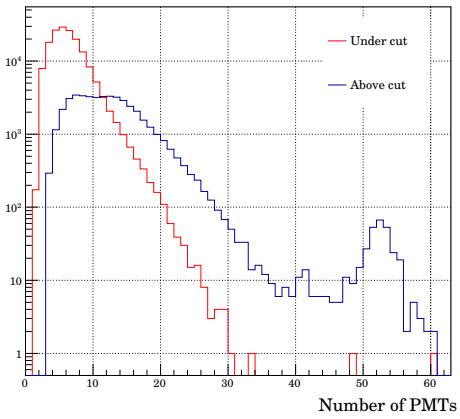

(a) Background data.

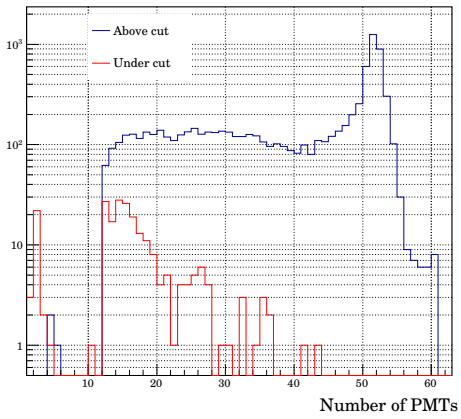

(b) Signal data.

Figure 5.5: Frequency plot of the number of PMT hit. The spectrum is split in the two subset given by the cut rule in Eq. 5.2.

Table 5.3: False positive counted with the help of Eq. 5.2. The Ratio columns for is the proportion of "under" and "above" counts with respect to the totality of pulses for signals and backgrounds respectively.

	Signal				Background			
Label	Total	Under	Above	Ratio (%)	Total	Under	Above	Ratio (%)
C	8 078	224	7 854	2.8	209 452	164 787	44 665	21.3
V_{00}	14 210	5 839	8 371	41.1	211 202	197 338	13 864	6.6
V_{01}	11 362	2 824	8 537	24.9	211 177	189 744	21 433	10.19
V_{05}	5 590	3	5 587	0.1	106 050	63 881	42 169	39.8
V_{10}	5 056	1	5 055	0.0	59 690	31 404	23 230	38.9
N_{15}	6 692	84	6 608	1.3	209 465	163 808	45 657	21.8
N_{30}	4 980	28	4 952	0.6	209 494	162 540	46 954	22.4
N_{50}	458	1	457	0.2	209 549	158 370	51 179	24.4
Δ_{50}	8 079	230	7 846	2.8	209 427	163 232	46 327	22.1
Δ_{30}	8 095	232	7 862	2.9	209 479	164 312	45 200	21.6
Δ_{20}	8 122	260	7 863	3.2	209 512	164 642	44 837	21.4
Δ_{10}	8 135	289	7 849	3.6	209 559	165 821	44 606	21.3

5.2 Results with the Beam run

5.2.1 Beam event selection

The spectrum in Fig. 5.6 is the first run taken with the MRD DAQ. It corresponds to 3.5×10^5 s of acquisition (nearly four days). As explained in section ref, only the second and the third layers are instrumented in phase I. The resolution of the TDCs is set to the maximum value available (4.0 ns), therefore the time window is 4.088 μs long. This suffices the aim of this preliminary test, i.e. to observe the beam by muon detection. The events collected are 64 298, resulting in nearly 0.2 events per seconds on average. The spectrum exhibits an augmentation, since it rises to an average value of (86.3 ± 0.5) from (45.6 ± 0.4) and (48.9 ± 0.4) respectively before and after it. These last two means are far from being compatible with the middle one, hence the contour of the spectrum can be implied to the presence of the beam. The increase happens from 1.124 μs to 2.648 μs in the TDC time window: the beam is 1.524 μs wide, in agreement with the effective total duration of the spill, which is 1.6 μs. As illustrated in Fig. 5.7, the beam events happen indeed from 10.2 to 11.8 microseconds.

Changing the analysis software parameters, the proportion between signals and backgrounds varies consequently. Beam neutrinos interacting in the water volume are likely to produce an outgoing muon along the beam direction (CCQE scattering). These kind of events are supposed not to have a coincidence signal with the veto. On the other hand, if the veto is triggered, then a non-decayed muon has probably passed through the detector. The lepton is expected to fire the MRD, therefore only pulses with an MRD coincidence are considered. Selecting data with this feature should reduce the number of backgrounds. Most of the pulses are tagged as signals, if the background rejection is efficient. The results on the Beam run are reported in Tab 5.4. Even if the pulses with a veto coincidence seems to outperform the pulses without the veto, in relation to signal to background ratio, the latter present a more limited variation to different thresholds.

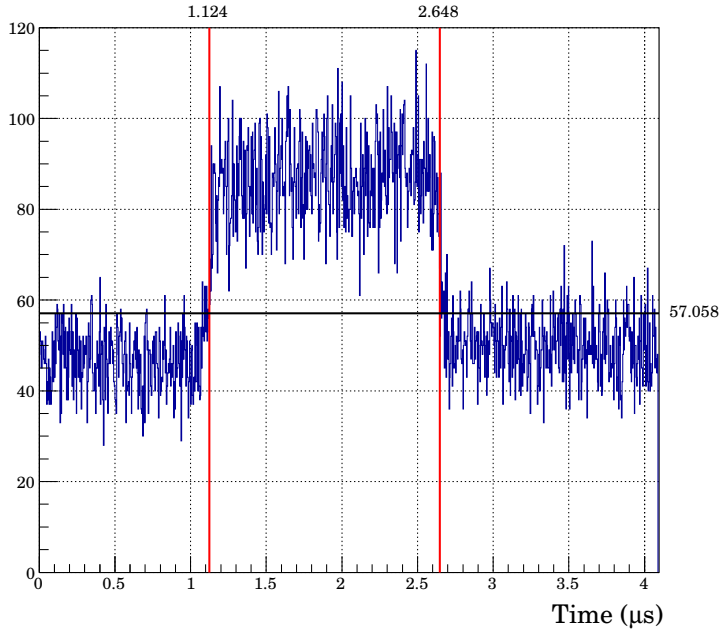

Figure 5.6: The time spectrum of the Beam run, seen by the MRD. The black line represents the arithmetic mean of the frequencies (y-axis), estimated to be 57.1 ± 0.2. The red lines at 1.124 and 2.648 are respectively the last and first intersection of the black line with the spectrum, in correspondence of the beam.

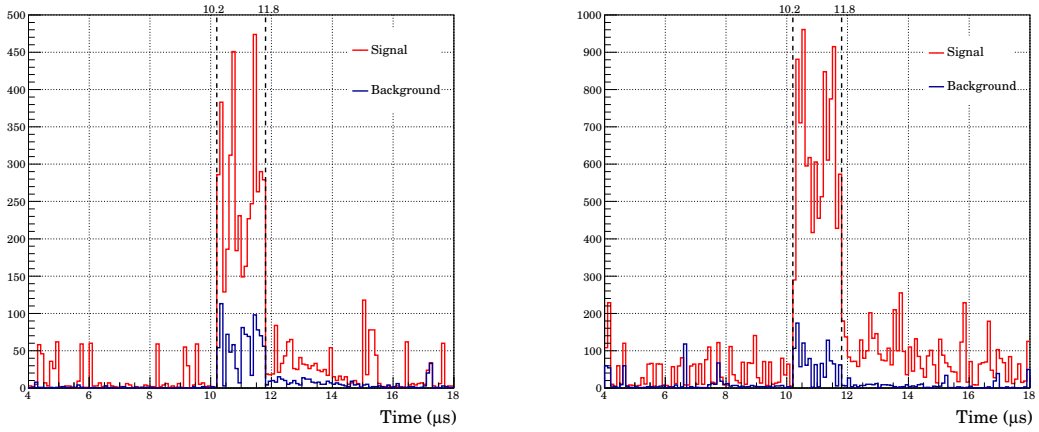

(a) Pulses without the veto coincidence.

(b) Pulses with the veto coincidence.

Figure 5.7: Time spectrum of the *Starts* from the Beam run, split for signals and backgrounds. The beam occurs between 10.2 μs and 11.8 μs.

Table 5.4: Count of beam events with an MRD coincidence. The Ratio columns are the ratio between the number of signals and the totality of pulses.

	Veto off				Veto on			
Label	Total	Signal	Background	Ratio (%)	Total	Signal	Background	Ratio (%)
C	5 176	4 254	922	82.2	11 292	10 197	1 095	90.3
V_{00}	6 480	4 232	2 248	65.3	14 041	10 372	3 669	73.9
V_{01}	6 527	4 583	1 944	70.2	12 885	10 504	2 381	81.5
V_{05}	1 034	1 033	1	99.9	73	59	14	80.8
V_{10}	0	0	0	N/A	0	0	0	N/A
N_{15}	5 070	4 179	891	82.4	10 909	10 048	861	92.1
N_{30}	4 998	4 038	960	80.8	10 769	9 673	1 096	89.9
N_{50}	4 724	3 780	1 398	80.0	10 342	7 904	2 438	76.4
Δ_{50}	5 378	4 505	873	83.8	11 724	10 626	1 098	90.6
Δ_{30}	5 178	4 272	906	82.5	10 399	9 245	1 154	88.9
Δ_{20}	5 148	4 095	1 053	79.5	9 700	7 973	1 727	82.2
Δ_{10}	5 178	3 780	1 398	73.0	9 004	6 055	2 949	67.2

5.2.2 Muon decay

As explained in section ref, the dominant decay channel of the muon is the *Michel decay*, which is reported in Eq. 1.30 and 1.31. The muon lifetime is a well known physical quantity and measured to be on average

$$\tau_{\text{avg}} = (2.196\,981\,1 \pm 0.000\,002\,2)\ \mu\,. \tag{5.3}$$

There is basically no discrepancy between μ^- and μ^+ lifetime in vacuum, respectively τ_{μ^-} and τ_{μ^+}. It has been measured that

$$\frac{\tau_{\mu^+}}{\tau_{\mu^-}} = 1.000\,024 \pm 0.000\,078\,. \tag{5.4}$$

However, the lifetimes can be significantly different in matter. A negative muon can form muonic atoms in matter and subsequent goes under nuclear capture. When this happens, new decay channels are favoured, thus reducing its lifetime, which depends on the atomic number of the material. The lifetime is ~ 2.0 μs in carbon, the Z of which is close to oxygen's. On the contrary, the positive muon always decay into a positron and two neutrinos, and its lifetime is the same as the vacuum one.

It is possible that a muon, either a cosmic one or produced in a CCQE interaction, decays inside ANNIE's volume, and the daughter electron is ejected with a velocity above the Cherenkov threshold ($E \gtrsim 772\ keV$): in this case, the electron can be detected. Measuring the abundance of electrons produced in such way, the muon lifetime can be inferred. Observing the time spectrum of the Beam run in Fig. 5.8, an exponential tail is found after the beam position, particularly accentuated for signals. No cut on the MRD or veto coincidence was done. The histogram can be fitted with the function:

$$y = N\mathrm{e}^{-x/\tau} + c_E\,. \tag{5.5}$$

On the contrary, the background pulses show a gaussian distribution right after the beam occurrence, which can be fitted with:

$$y = A\exp\left(-\frac{(x-\mu)^2}{2\sigma^2}\right) + c_N\,. \tag{5.6}$$

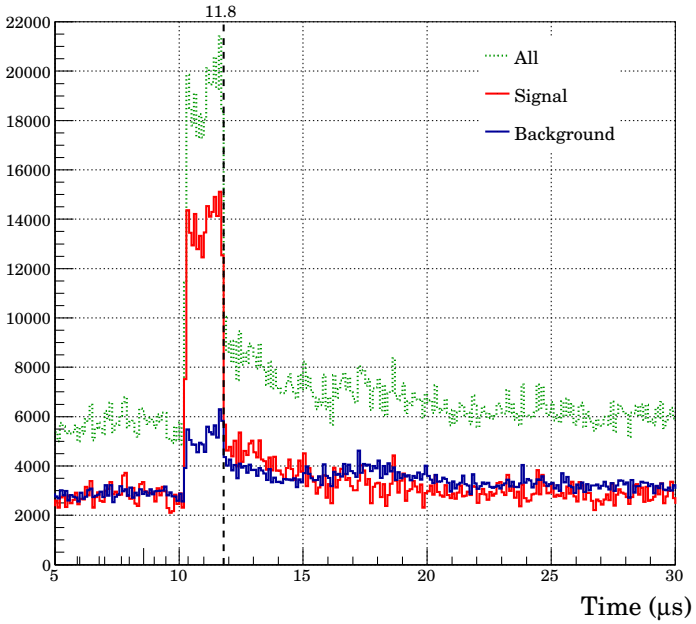

Figure 5.8: The time spectrum of the Beam run has been split between signals and backgrounds. After the beam position, an exponential tail is visible for signals, while there is a gaussian peak in backgrounds. The plot of all data should present a tail which follow the sum of an exponential and a gaussian distribution.

Therefore the spectrum, realised without distinguishing between signals and backgrounds, may be fitted with the sum of Eq. 5.5 and Eq. 5.6:

$$y = N_{\mathrm{T}} \mathrm{e}^{-x/\tau_{\mathrm{T}}} + A_{\mathrm{T}} \exp\left(-\frac{(x-\mu_{\mathrm{T}})^2}{2\sigma_{\mathrm{T}}^2} \right) + c_{\mathrm{T}} \,. \tag{5.7}$$

Regarding Eq. 5.5, the τ parameter should be compatible with the muon lifetime, while the gaussian peak of Eq. 5.6 is supposedly the afterpulsing of the PMTs. In Tab. 5.5, the fitted values of these two parameters are reported. The fit results are reviewed in their entirety in App. D. Mostly positive muons are presumed to be produced in the chain of the beam reactions, so the muon lifetime is expected to be close to its value in vacuum. The most compatible values of the measured lifetime with τ_{avg} are given by V_{05}, V_{10}, Δ_{20}, and Δ_{10}, because the time correlation between pulses in these data sets is stricter and other effects, such as reflection, are neglected.

5.2.3 Neutron yield

The PMT mounted on top of the NCV is able to detected the scintillation light and is analysed just as the other detectors, but the signal discrimination is skipped. A neutron capture by gadolinium is expected to release 8 MeV, detectable even by the tubes on the bottom of the tank. Only signals within 20 ns from the NCV pulse are considered in the Beam run, in particular their time delay with respect to the beam position. Even if a fit of data is not feasible, due to the large RMS, studying the mean and the standard deviation could unveil some information regarding the distribution of the events. This is allowed by the exponential distribution, typical of the neutron capture, because its PDF is $\lambda \mathrm{e}^{-\lambda x}$, which has a mean of $1/\lambda$ and a variance of $1/\lambda^2$. The mean is computed to be

Table 5.5: Fit results of the τ and μ parameter of respectively Eq. 5.5, for the signal part of the spectrum, and Eq. 5.6, for the background one. The entire spectrum is also fitted, with Eq. 5.7, and the two parameters are inferred.

Label	Signal τ (μs)	Background μ (μs)	Total τ_{T} (μs)	Total μ_{T} (μs)
C	2.94±0.06	17.66±0.05	3.2±0.1	18.13±0.05
V_{00}	4.25±0.04	17.85±0.03	4.29±0.09	17.76±0.02
V_{01}	4.02±0.03	17.73±0.03	4.66±0.09	17.78±0.03
V_{05}	2.8±0.2	18.16±0.05	1.8±0.2	18.10±0.09
V_{10}	2.16±0.05	18.22±0.06	9.3±0.7	17.397±0.002
N_{15}	3.06±0.07	17.61±0.04	4.7±0.2	18.24±0.06
N_{30}	3.07±0.09	17.56±0.06	3.4±0.1	18.26±0.05
N_{50}	3.3±0.1	17.76±0.07	5.31±0.08	17.81±0.02
Δ_{50}	2.48±0.02	18.03±0.04	3.5±0.1	18.16±0.05
Δ_{30}	2.64±0.07	17.04±0.07	3.8±0.1	18.17±0.05
Δ_{20}	2.07±0.04	17.65±0.06	2.76±0.08	18.03±0.05
Δ_{10}	2.09±0.04	17.60±0.05	3.8±0.1	18.17±0.05

around 30 μs, while the dispersion is close to 21 μs, as summarised in Tab. 5.6. This two values are not compatible with each other, in agreement with the expected distribution, but are rather compatible with the uniform distribution. In fact, considering the events after the beam, the available interval is roughly 70 μs, hence the mean is 35 μs and the standard deviation is nearly 20 μs. For the precious reasons is not possible to draw conclusions on neutron observation.

The average shape of the signals produced by the scintillator is illustrated in Fig. 5.9 and compared with the signal and the background average pulse.

Table 5.6: The pulses acquired from the PMT of the NCV were counted. The arithmetic average of their time position with respect to the time occurrence of the beam and their deviation from the mean are also calculated.

Label	NCV	Mean (μs)	RMS (μs)
C	6677	30.2 ±0.3	22.1 ±0.2
V_{00}	20197	30.0 ±0.1	20.6 ±0.1
V_{01}	14726	30.5 ±0.2	20.8 ±0.1
V_{05}	2036	30.8 ±0.5	21.3 ±0.3
V_{10}	416	25 ±1	21.2 ±0.7
N_{15}	6456	29.9 ±0.3	22.2 ±0.2
N_{30}	6036	30.8 ±0.3	22.1 ±0.2
N_{50}	5661	31.2 ±0.3	22.3 ±0.2
Δ_{50}	6531	30.2 ±0.3	22.2 ±0.2
Δ_{30}	7196	30.0 ±0.3	21.8 ±0.2
Δ_{20}	7288	30.2 ±0.3	21.7 ±0.2
Δ_{10}	7302	30.1 ±0.3	21.7 ±0.2

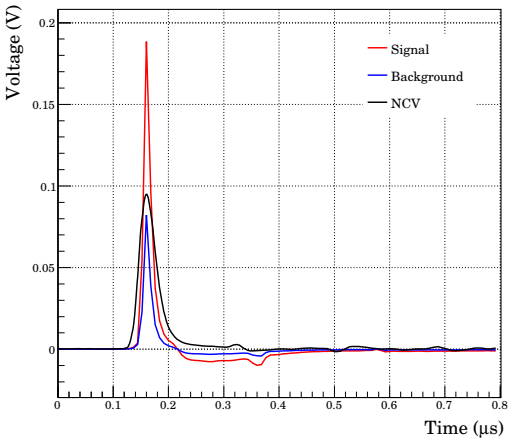

Figure 5.9: Average pulses of the Beam run in comparison with the pulses collected from the NCV.

Chapter 6

Conclusions

The ANNIE experiment provides an opportunity to make an important measurement of the final-state neutron abundance from neutrino interactions with water nuclei as a function of momentum transfer. This measurement will have a significant impact on a variety of future physics analyses. To that end, the R&D of phase I is a crucial step to provide all the necessary tools.

The current DAQ has proven to be a reliable and stable system, even for long acquisition sessions. The modularity of the *ToolDAQ* framework is for sure one of its greatest advantage, on the software side, allowing versatility and fast improvements. With this in mind, the acquisition system for the MRD has been developed with good results. The MRD DAQ is solid and has an uninfluential dead time, even though the detector is partially employed. The system can be easily upgraded when the detector will be fully instrumented, thanks to the scalability of the software. In the next stage of the experiment, the Main DAQ and the MRD DAQ will acquire data simultaneously.

The data analysis procedures presented in Chapter 4 is far from being definitive, but sets the basis for a versatile analysis framework. Collecting and arranging individual pulse not only help to spare storage size, but also give a handle on the relevant fraction of data, ignoring the unmeaningful part. The analyses undertaken in Chapter 5 confide in a correct signal discrimination from background, which in turn depends on the three variables, V_T, N_{PMT}, and Δ_T. Setting these three values properly is possible to prepare raw data for more advanced analysis. Twelve different combination were used with which a cosmic event run and a beam event run were studied, in relation to cosmics rate, muon decay, and neutron yield. It has been found that a voltage threshold of 0.02 V does not preclude any important physical information, and is a good compromise with respect to data size. The values chosen for Δ_T do not have a great influence on the discrimination. The time rejection window should be redefined as a left-bounded interval from the peak onward, with reference to Fig. 4.6. On the contrary, it is more difficult to come to a conclusion on N_{PMT}. A high threshold would be sensitive predominantly to cosmic muons, whereas a low number of coincidences could lead to a misinterpretation of the signals. This issue is due to the current disposition of the PMTs, and it will be overcome with ease in the future phases of ANNIE, when the the photocoverage will be considerably expanded.

Appendix A

Booster Neutrino Beam

FNAL has two major neutrino beam lines: the Neutrino Main Injector (NuMI) and the Booster Neutrino Beam (BNB). The energy range of these two neutrino sources on-axis is in the GeV range, which is too high to satisfy the condition for dominance of coherent scattering. The BNB source has substantial advantages over the NuMI beam source owing to suppressed kaon production from the relatively low energy 8 GeV proton beam on the target [29]. Therefore, pion decay and subsequent muon decay processes are the dominant sources of neutrinos. At the far-off-axis area, the detector can be placed close enough to the target to gain a large increase in neutrino flux due to the larger solid angle acceptance. Moreover, the far-off-axis ($> 45°$) of the BNB produces more defined neutrinos, with energies below 50 MeV [41].

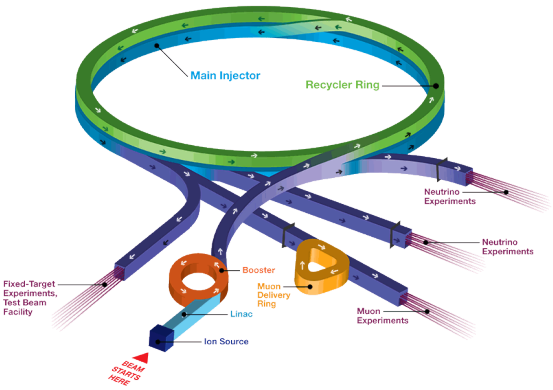

Figure A.1: FNAL accelerator complex.

The Booster is a 474-metre-circumference synchrotron operating at 15 Hz. All the protons are extracted by a fast-rising kicker from the Linac and injected into the BNB. These are then accelerated from 400 MeV to 8 GeV kinetic energy, or 8.89 GeV/c momentum, by the Booster. Even if the BNB has a harmonic number of 84, the beam is structured in a series of 81 proton bunches each 2 ns wide and 19 ns apart. Upon leaving the Booster, the proton beam is transported through a lattice of focusing and defocusing quadrupoles (FODO) and dipole magnets. A switch magnet steers the beam to the main injector or to the BNB. The BNB is also a FODO that terminates with a triplet that focuses the beam on the target. The maximum allowable average repetition rate for delivery of protons to the BNB is 5 Hz (with a maximum of 11 pulses in a row at 15 Hz) and 5×10^{12} protons per pulse. The 5 Hz limit is set by the design of the horn and its power supply [29].

A.1 The target

The target is made of beryllium divided in seven cylindrical sections in a total of 71.1 cm, in length, or about 1.7 inelastic interaction length, and 0.51 cm in radius. The target is contained within a beryllium sleeve 0.9 cm thick with an inner radius of 1.37 cm.

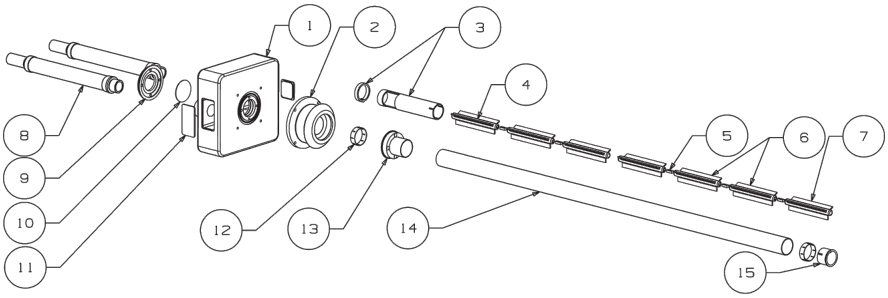

Figure A.2: An exploded view of the beryllium target assembly. 1) target base block; 2) bellow contact system; 3) upstream target slug locator and ring; 4) target slug, upstream; 5) target slug pin; 6) target slug, middle; 7) target slug, downstream; 8) air cool standoff; 9) window flange; 10) beryllium window; 11) base plug; 12) lock ring; 13) outer tube flange; 14) outer tube; 15) on-stream target slug locator and gasket. Figure taken from [29]

Each target slug is supported within the sleeve by three "fins" (also beryllium) which extend radially out from the target to the sleeve. The volume of air within the sleeve is circulated to provide cooling for the target when the beam line is in operation. An exploded view of the various components, with the downstream end of the target on the right, is outlined in Fig. A.2. The choice of Be as the target material was motivated by residual radioactivity issues in the event that the target assembly needed to be replaced, as well as energy loss considerations that allow the air-cooling system to be sufficient. The vacuum of the beam pipe extends to about 150 centimetres upstream of the target, minimising upstream proton interactions [29].

A.2 The Horn

The horn, shown in Fig. A.3, is a pulsed toroidal electromagnet composed of an aluminium alloy, which surrounds the target. This device bends, sign-selects, and focuses the secondary particles that emerge from the interactions in the beryllium, along the direction pointing to the detector. The current flowing in the horn is a 143 μs-long pulse half sinusoid, with a nominal amplitude of 170 kA coinciding with the arrival of the proton beam at the target. The actual operating values are typically 174 kA in both neutrino mode (positive current) and antineutrino mode (negative current), with ± 1 kA variations. In neutrino mode, the flow of current runs along the inner conductor, which folds outwards at a length of 185 cm to return via the outer conducting cylinder of the horn at 30 cm radius. The pulse creates a magnetic field within the horn cavity that falls as $1/R$, where R is the distance from the cylindrical symmetry axis of the horn. The largest magnetic field values of 1.5 T are obtained where the inner conductor is the narrowest (2.2 cm radius). The "skin effect", in which the time-varying currents travelling on the surface of the conductor penetrate into the conductor, results in electromagnetic fields within the conductor itself. However, the effects of time-varying fields in the cavity are found to be negligible [29]. The target assembly is rigidly fixed to the upstream face of the horn, although the target is electrically isolated from its current path.

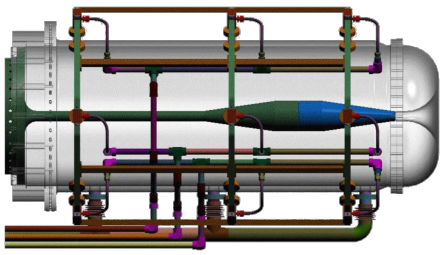

Figure A.3: BNB horn system. Figure taken from [29]

The beam of focused, secondary mesons emerging from the target/horn region is further collimated, via passive shielding, and allowed to decay into neutrinos in a cylindrical decay region filled with air at atmospheric pressure, 50 m long and 90 cm in radius. A beam absorber, made of steel and concrete and located at the end of the decay region, stops the hadronic and muonic component of the beam, and only a pure neutrino beam pointing toward the detector remains, mostly from the process $\pi \rightarrow \mu + \nu_\mu$.

A.3 Monitoring

Upstream of the target, the primary proton beam is monitored using four systems:

- two toroids measuring its intensity (protons per pulse);
- beam position monitors (BPM);
- a multiwire chamber, that in combination with the BPMs determines the width and position of the beam;
- a resistive wall monitor (RWM) measuring both the time and intensity of the beam spills.

The number of protons delivered to the BNB target is measured for each proton batch using the toroids located near the target along the beam line. The toroids are continuously calibrated at 5 Hz with their absolute calibrations verified twice a year. The calibrations have shown minimal deviation ($< 0.5\,\%$). The proton flux measured in the two toroids agree to within 2%, compatible with the expected systematic uncertainties.

The BPMs are split-plate devices that measure the difference of charge induced on two plates. By measuring the change in beam position at several locations without intervening optics, the BPMs are found to be accurate to 0.1 mm. The typical beam alignment and divergence measured by the beam profile monitors located near the target are within 1 mm and 1 mrad of the nominal target centre and axis direction, respectively. These parameters are well within the experiment requirements. The multiwire is a wire chamber with 48 horizontal and 48 vertical wires and 0.5 mm pitch. The profile of the beam is measured using the secondary emission induced by the beam on the wires.

The RWM is located upstream of the target to monitor the time and intensity of the proton pulses prior to hitting the target, by measuring the image charge that flows along the vacuum chamber following the beam. The image charge has equal magnitude but opposite sign and in order to measure it, the beam pipe is cut and a resistive gap is inserted. Depending on the beam velocity, the image charge will lag behind and be spread out along its path. The ultimate bandwidth of such a detector is limited by this spreading of the electric field lines between the beam and the inside walls of the beam pipe. Various ferrite cores are used to force the image current through the resistive gap rather than allowing it to flow through other conducting paths [42].

Appendix B

Cosmic muons

High energy particles, mainly originated outside the Solar System and thus called *Cosmic Rays*, impact on the Earth's atmosphere and produce mesons, which in turn generate secondary particle shower by decaying. The primary particles are about 99 % made of ionised nuclei (whose 86 % made of protons, 12.7 % of helium nuclei, and 1.3 % of heavier nuclei), while the remaining 1 % is mostly composed by electrons [43]. The intensity of the nucleons in the energy range from several GeV to somewhat beyond 100 TeV is given approximately by

$$I_N(E) \simeq 1.8 \times 10^4 \left(\frac{E}{1\ Gev} \right)^{-\alpha} \frac{\text{nucleons}}{\text{m}^2\,\text{s}\,\text{sr}\,\text{Gev}}\,, \tag{B.1}$$

where E is the energy-per-nucleon, including rest mass energy, and $\alpha = 2.7$ is the differential spectral index of the cosmic ray flux. There are many secondary products reaching the sea level, among which muons, neutrinos, nucleons, and electrons. The first two, muons and neutrinos, derive from the decay chain of charged mesons, while electrons and photons originate in decays of neutral mesons. As Fig. B.1 shows, muons are the most numerous charged particles at sea level. The direction of propagation is the same as that of their parents pions and in average they receive close to 80 % of their parent's energy. They are very penetrating because their nuclear interaction cross section is only about 2×10^{-29} cm^2 (two microbarns). The energy loss to ionisation is at a fairly constant rate of about 2 MeV per g/cm^2. Given that the vertical depth of the atmosphere is about 1000 g/cm^2, muons will lose about two GeV before reaching the ground. The mean energy of muons at sea level is about four GeV; therefore the mean energy at creation, typically fifteen kilometres high, is probably near six GeV. Their energy and angular distribution reflect a convolution of the production spectrum, energy loss in the atmosphere, and decay. The integral intensity of vertical muons above 1 GeV/c at sea level is nearly

$$I_{\text{MSL}} \simeq 70\ \text{m}^{-2}\text{s}^{-1}\text{sr}^{-1}\,, \tag{B.2}$$

for horizontal detectors. The overall angular distribution of muons at the ground behaves as:

$$\frac{\text{d}N}{\text{d}A\Omega\text{d}t} \propto \cos^k\theta\,, \tag{B.3}$$

where $k \simeq 2$. There is no expected dependence on the azimuthal angle ϕ, while the above relation is not expected to be valid for $\theta > 80^\circ$ where the Earth's curvature becomes an important consideration. However, integrating with respect to the solid angle, with a

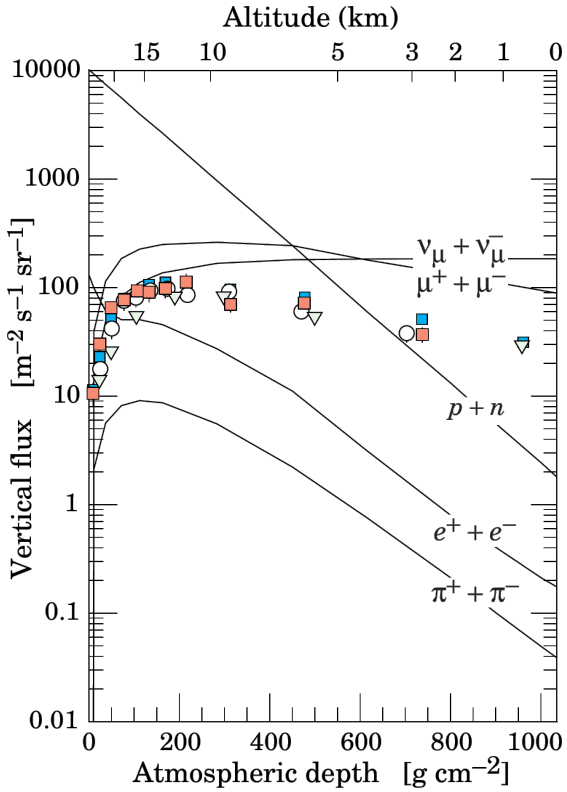

Figure B.1: Vertical fluxes of cosmic rays in the atmosphere with $E > 1$ GeV estimated from the nucleon flux of Eq. B.1. The points show measurements of negative muons with 1 GeV. Picture taken from [7].

zenith angle $0 < \theta < \pi/2$, it is possible to estimate the rate of muons per area unit:

$$I_0 = 2\pi I_{\mathrm{MSL}} \int_0^{\pi/2} \cos^2\theta \sin\theta \mathrm{d}\theta = \frac{2}{3}\pi I_{\mathrm{MSL}} \simeq 147 \text{ Hz m}^{-2}\,, \tag{B.4}$$

Appendix C

Monte Carlo simulation

A simple Monte Carlo simulation was developed in order to help study the Cherenkov radiation production to the passage of a charged particle. The minimal model to study the distribution of the photon on the floor of the tank and the role of the walls is implemented. This considers only vertical muons with $\beta = 1$, and both scattering with nucleons and the related energy loss are ignored. A uniform Mersenne Twister (MT) generator[1] defines the position of the muon entering in the tank. It propagation is stopped every 0.1 cm and a handful of photons is generated isotropically, using the same PRNG. The number of photons at each step is fixed a priori and Eq. 2.2 gives:

$$N_\gamma \simeq 27\,, \tag{C.1}$$

with $L = 0.1$ cm, θ_C maximum, and λ interval from 300 to 500 nm. As soon as all the photons ends their route, the muon is moved and the process is repeated again, until even the charged lepton hits the bottom.

The track of the gammas is precisely defined by its origin, the direction it is emitted, and the reflection coefficient of the PVC walls, because they travel in straight lines. With elementary geometry, it is easy to calculate the track of the photons. Since the muon travels at ultrarelativistic speed, the wavefront of the photons has the maximum angle allowed by the Cherenkov effect, which in water is $\theta_C = 41°$. The muon and the photons tracks are exemplified in Fig. C.1. The impact of the walls is managed by the same MT generator.

For every reflection coefficient, hundred muons are simulated and some illustrative results are shown in Fig. C.2. Being the tank 4 metres tall, the muon makes 4000 steps, hence 108 000 photons are generated every time. Obviously only when the walls entirely reflects (100 % reflection), all the photons reach the bottom. Despite its simplicity, this model is capable of producing interesting results.

[1]The Mersenne Twister is a pseudorandom number generator (PRNG) and its name is due to the fact that its period length is a Mersenne prime. The version used employes the Mersenne prime $2^{219937} - 1$.

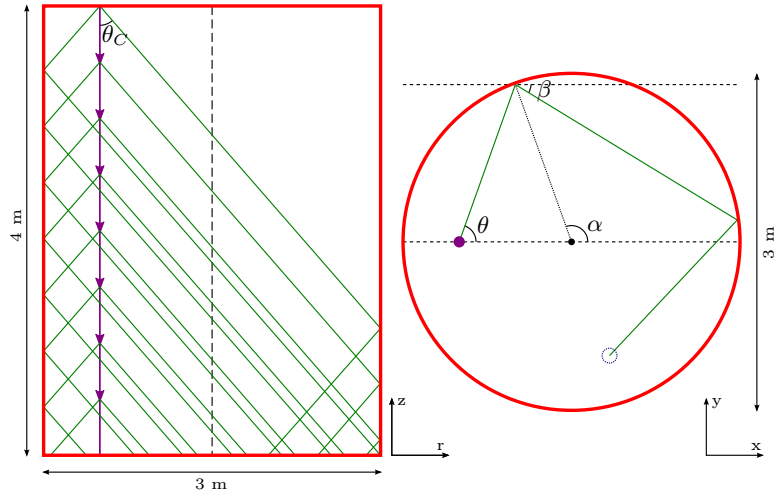

Figure C.1: Track of the incoming muon (in purple) and the emitted photons (in green). On the left, the side view underlines the angle of the wavefront with respect to the z-axis, θ_C. On the right, the top view shows the xy-plane reflections of the photon. Since θ and α are known, the angle after the reflection is $\beta = \pi - \theta + 2\alpha$.

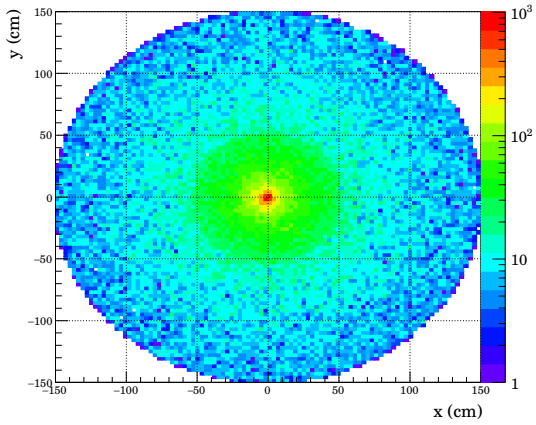

(a) Muon at the centre of the cylinder and 100 % wall reflection.

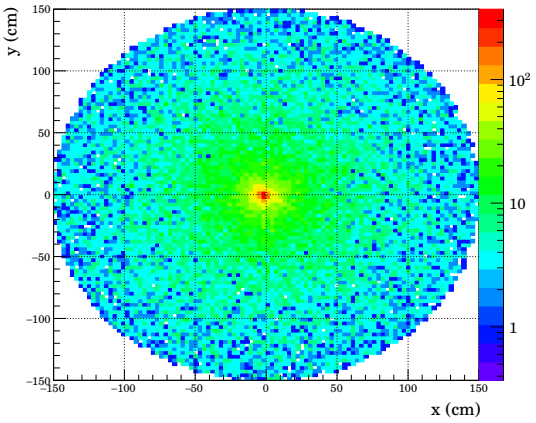

(b) Muon at the centre of the cylinder and 0 % wall reflection.

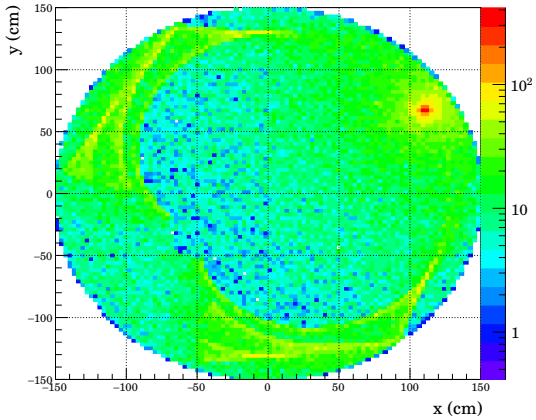

(c) Muon at a distance greater than 120 cm from the centre and 100 % wall reflection.

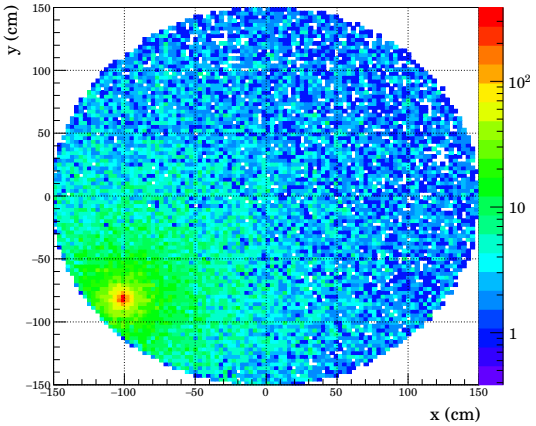

(d) Muon at a distance greater than 120 cm from the centre and 0 % wall reflection.

Figure C.2: Pattern created by the photons deposited on the bottom of the water tank. Wall reflection and distance from the centre influence the distribution.

Appendix D

Fit results

In this appendix, the fit result mentioned in section 5.2.2 are reported in their entirety.

D.1 Signal

The behaviour of the event spectrum is exponential, thereby the following function was fitted:

$$y = N\mathrm{e}^{-x/\tau} + c_E\,, \tag{D.1}$$

with τ in μs.

C

Correlation matrix				Best fit		
	N	$1/\tau$	c_E	Value	Error	Err(%)
N	1.000	−0.996	0.532	12.43	0.09	0.72
$1/\tau$	−0.996	1.000	−0.563	−0.340	0.007	2.06
c_E	0.532	−0.563	1.000	5 756	8	0.14

V_{00}

Correlation matrix				Best fit		
	N	$1/\tau$	c_E	Value	Error	Err%
N	1.000	−0.989	0.508	12.43	0.03	0.24
$1/\tau$	−0.989	1.000	−0.568	−0.340	0.002	0.59
c_E	0.508	−0.568	1.000	10.18×10^3	0.01×10^3	0.10

V_{01}

Correlation matrix				Best fit		
	N	$1/\tau$	c_E	Value	Error	Err%
N	1.000	−0.990	0.446	12.05	0.03	0.25
$1/\tau$	−0.990	1.000	−0.518	−0.249	0.002	0.80
c_E	0.446	−0.518	1.000	8 701	9	0.10

V_{05}

Correlation matrix				Best fit		
	N	$1/\tau$	c_E	Value	Error	Err%
N	1.000	−0.996	0.434	11.4	0.2	1.75
$1/\tau$	−0.996	1.000	−0.462	−0.36	0.02	5.56
c_E	0.434	−0.462	1.000	3 594	5	0.13

V_{10}

Correlation matrix				Best fit		
	N	$1/\tau$	c_E	Value	Error	Err%
N	1.000	−0.858	0.709	6.0	0.1	1.67
$1/\tau$	−0.858	1.000	−0.963	−0.46	0.01	2.17
c_E	0.709	−0.963	1.000	2.57×10^3	0.02×10^3	0.78

N_{15}

Correlation matrix				Best fit		
	N	$1/\tau$	c_E	Value	Error	Err%
N	1.000	−0.997	0.539	12.2	0.1	0.82
$1/\tau$	−0.997	1.000	−0.567	−0.327	0.008	2.45
c_E	0.539	−0.567	1.000	5 488	7	0.13

N_{30}

Correlation matrix				Best fit		
	N	$1/\tau$	c_E	Value	Error	Err%
N	1.000	−0.996	0.560	11.8	0.1	0.85
$1/\tau$	−0.996	1.000	−0.562	−0.326	0.01	3.07
c_E	0.560	−0.592	1.000	5 103	8	0.16

N_{50}

Correlation matrix				Best fit		
	N	$1/\tau$	c_E	Value	Error	Err%
N	1.000	−0.996	0.497	11.1	0.1	0.90
$1/\tau$	−0.996	1.000	−0.527	−0.30	0.01	3.33
c_E	0.497	−0.527	1.000	4 085	5	0.12

Δ_{50}

Correlation matrix				Best fit		
	N	$1/\tau$	c_E	Value	Error	Err%
N	1.000	−0.997	0.406	11.35	0.08	0.70
$1/\tau$	−0.997	1.000	−0.427	−0.403	0.006	1.49
c_E	0.406	−0.427	1.000	6 055	6	0.10

Δ_{30}

Correlation matrix				Best fit		
	N	$1/\tau$	c_E	Value	Error	Err%
N	1.000	−0.999	0.620	12.9	0.2	1.55
$1/\tau$	−0.999	1.000	−0.633	−0.38	0.01	2.64
c_E	0.620	−0.633	1.000	5 337	7	0.13

Δ_{20}

Correlation matrix				Best fit		
	N	$1/\tau$	c_E	Value	Error	Err%
N	1.000	−0.998	0.394	14.1	0.1	0.71
$1/\tau$	−0.998	1.000	−0.409	−0.48	0.01	2.08
c_E	0.394	−0.409	1.000	4 295	5	0.12

Δ_{10}

Correlation matrix				Best fit		
	N	$1/\tau$	c_E	Value	Error	Err%
N	1.000	−0.998	0.335	13.6	0.2	1.47
$1/\tau$	−0.998	1.000	−0.352	−0.48	0.01	2.08
c_E	0.335	−0.352	1.000	3 346	4	0.12

D.2 Background

The behaviour of the event spectrum is exponential, thereby the following function was fitted:

$$y = A \exp\left(- \frac{(x-\mu)^2}{2\sigma^2} \right) + c_N \,, \tag{D.2}$$

with μ and σ in μs.

C

Correlation matrix					Best fit		
	A	μ	σ	c_N	Value	Error	Err%
A	1.000	0.170	0.574	−0.150	1.43×10^3	0.03×10^3	2.10
μ	0.170	1.000	0.321	0.010	17.66	0.05	0.28
σ	0.574	0.321	1.000	0.364	2.03	0.07	3.45
c_N	−0.150	0.010	0.364	1.000	6 312	9	0.14

V_{00}

Correlation matrix					Best fit		
	A	μ	σ	c_N	Value	Error	Err%
A	1.000	0.038	−0.615	−0.078	4.16×10^3	0.06×10^3	1.44
μ	0.038	1.000	−0.062	−0.064	17.85	0.03	0.17
σ	−0.615	−0.062	1.000	−0.435	2.24	0.06	2.68
c_N	−0.078	−0.064	−0.435	1.000	29.87×10^3	0.02×10^3	0.07

V_{01}

Correlation matrix					Best fit		
	A	μ	σ	c_N	Value	Error	Err%
A	1.000	0.082	−0.670	−0.030	3.53×10^3	0.05×10^3	1.42
μ	0.082	1.000	−0.154	−0.031	17.73	0.03	0.17
σ	−0.670	−0.154	1.000	−0.391	2.18	0.06	2.68
c_N	−0.030	−0.031	−0.391	1.000	29.84×10^3	0.01×10^3	6.70

V_{05}

Correlation matrix					Best fit		
	A	μ	σ	c_N	Value	Error	Err%
A	1.000	0.074	−0.545	−0.138	0.58×10^3	0.01×10^3	1.72
μ	0.074	1.000	−0.120	0.023	18.16	0.05	0.28
σ	−0.545	−0.120	1.000	−0.351	1.85	0.06	3.24
c_N	−0.138	0.023	−0.351	1.000	1 411	4	0.28

V_{10}

Correlation matrix

	A	μ	σ	c_N
A	1.000	0.164	−0.491	−0.157
μ	0.164	1.000	−0.319	0.119
σ	−0.491	−0.319	1.000	−0.389
c_N	−0.157	0.119	−0.389	1.000

Best fit

Value	Error	Err%
0.29×10^3	0.01×10^3	3.49
18.22	0.06	0.33
1.58	0.07	4.43
653	3	0.46

N_{15}

Correlation matrix

	A	μ	σ	c_N
A	1.000	0.105	−0.584	−0.144
μ	0.105	1.000	−0.182	−0.014
σ	−0.584	−0.182	1.000	−0.324
c_N	−0.144	−0.014	−0.324	1.000

Best fit

Value	Error	Err%
1.47×10^3	0.03×10^3	2.04
17.61	0.04	0.23
2.18	0.06	2.75
6 107	7	0.11

N_{30}

Correlation matrix

	A	μ	σ	c_N
A	1.000	0.416	−0.856	0.138
μ	0.416	1.000	−0.519	0.122
σ	−0.856	−0.519	1.000	−0.411
c_N	0.138	−0.122	−0.411	1.000

Best fit

Value	Error	Err%
1.44×10^3	0.04×10^3	2.78
17.56	0.06	0.34
2.8	0.1	3.57
6 177	8	0.13

N_{50}

Correlation matrix

	A	μ	σ	c_N
A	1.000	0.267	−0.597	−0.061
μ	0.267	1.000	−0.647	0.117
σ	−0.597	−0.647	1.000	−0.347
c_N	−0.061	0.117	−0.347	1.000

Best fit

Value	Error	Err%
1.50×10^3	0.03×10^3	2.00
17.76	0.08	0.45
2.1	0.1	4.76
6 850	8	0.12

Δ_{50}

Correlation matrix

	A	μ	σ	c_N
A	1.000	0.000	−0.644	−0.081
μ	0.000	1.000	−0.023	−0.043
σ	−0.644	−0.023	1.000	−0.246
c_N	−0.081	−0.043	−0.246	1.000

Best fit

Value	Error	Err%
1.38×10^3	0.03×10^3	2.17
18.03	0.04	0.22
1.88	0.06	3.19
5 871	5	0.09

Δ_{30}

Correlation matrix					Best fit		
	A	μ	σ	c_N	Value	Error	Err%
A	1.000	0.323	−0.641	−0.036	1.51×10^3	0.03×10^3	1.99
μ	0.323	1.000	−0.597	0.134	17.04	0.07	0.41
σ	−0.641	−0.597	1.000	−0.413	3.0	0.1	3.33
c_N	−0.036	0.134	−0.413	1.000	6 611	8	0.12

Δ_{20}

Correlation matrix					Best fit		
	A	μ	σ	c_N	Value	Error	Err%
A	1.000	0.215	−0.553	−0.120	1.68×10^3	0.03×10^3	1.79
μ	0.215	1.000	−0.550	0.081	17.65	0.06	0.34
σ	−0.553	−0.550	1.000	−0.384	2.20	0.08	3.64
c_N	−0.120	0.081	−0.384	1.000	7.70×10^3	0.01×10^3	0.13

Δ_{10}

Correlation matrix					Best fit		
	A	μ	σ	c_N	Value	Error	Err%
A	1.000	0.190	−0.571	−0.120	1.86×10^3	0.03×10^3	1.61
μ	0.190	1.000	−0.484	0.043	17.60	0.05	$0.28 thrms$
σ	−0.571	−0.484	1.000	−0.339	2.02	0.07	$3.47 thrms$
c_N	−0.120	0.043	−0.339	1.000	8 653	9	0.10

D.3 All data

The behaviour of the whole spectrum has two componente, an exponential and a gaussian one, thereby the following function was fitted:

$$y = N_{\mathrm{T}} \mathrm{e}^{-x/\tau_{\mathrm{T}}} + A_{\mathrm{T}} \exp\left(- \frac{(x-\mu_{\mathrm{T}})^2}{2\sigma_{\mathrm{T}}^2} \right) + c_{\mathrm{T}} \,, \tag{D.3}$$

with τ_{T}, μ_{T}, and σ_{T} in μs.

C

Correlation matrix

	A_T	μ_T	σ_T	N_T	$1/\tau_T$	c_T
A_T	1.000	−0.178	−0.236	0.733	−0.737	−0.329
μ_T	−0.178	1.000	−0.103	−0.103	0.110	−0.142
σ_T	−0.236	−0.103	1.000	−0.656	0.662	−0.263
N_T	0.733	−0.103	−0.656	1.000	0.999	0.544
$1/\tau_T$	−0.737	0.110	0.662	0.999	1.000	−0.558
c_T	−0.329	−0.142	−0.263	0.544	−0.558	1.000

Best fit

Value	Error	Err%
1.42×10^3	0.06×10^3	4.23
18.13	0.05	0.28
1.24	0.05	4.03
12.4	0.1	0.81
−0.31	0.01	3.23
12.00×10^3	0.01×10^3	0.08

V_{00}

Correlation matrix

	A_T	μ_T	σ_T	N_T	$1/\tau_T$	c_T
A_T	1.000	0.003	0.107	0.588	−0.597	0.426
μ_T	0.003	1.000	0.329	0.223	−0.218	0.114
σ_T	0.107	0.329	1.000	0.651	−0.661	0.454
N_T	0.588	0.223	0.651	1.000	−0.997	0.763
$1/\tau_T$	−0.597	−0.218	−0.661	−0.997	1.000	−0.783
c_T	0.426	0.114	0.454	0.763	−0.783	1.000

Best fit

Value	Error	Err%
5.2×10^3	0.1×10^3	1.92
17.76	0.02	0.11
1.01	0.03	2.97
12.49	0.07	0.56
−0.233	0.005	2.15
4.00×10^3	0.03×10^3	0.75

V_{01}

Correlation matrix

	A_T	μ_T	σ_T	N_T	$1/\tau_T$	c_T
A_T	1.000	−0.025	−0.051	0.496	−0.513	0.288
μ_T	−0.025	1.000	0.391	0.259	−0.255	0.111
σ_T	−0.051	0.391	1.000	0.527	−0.544	0.290
N_T	0.496	0.259	0.527	1.000	−0.995	0.607
$1/\tau_T$	−0.513	−0.255	−0.544	−0.995	1.000	−0.634
c_T	0.288	0.111	0.290	0.607	−0.634	1.000

Best fit

Value	Error	Err%
3.55×10^3	0.09×10^3	2.53
17.78	0.03	0.17
0.95	0.03	3.16
12.00	0.05	0.33
−0.215	0.004	1.86
29.33×10^3	0.02×10^3	0.07

V_{05}

Correlation matrix

	A_T	μ_T	σ_T	N_T	$1/\tau_T$	c_T
A_T	1.000	−0.401	−0.083	0.480	−0.479	−0.076
μ_T	−0.401	1.000	−0.543	−0.742	0.744	−0.099
σ_T	0.083	−0.543	1.000	0.768	−0.789	−0.076
N_T	0.480	−0.742	0.786	1.000	−1.000	0.071
$1/\tau_T$	−0.479	0.744	−0.789	−1.000	1.000	−0.075
c_T	−0.076	−0.099	−0.076	0.071	−0.075	1.000

Best fit

Value	Error	Err%
0.77×10^3	0.03×10^3	3.90
18.09	0.09	0.50
1.7	0.1	5.88
14.4	0.8	5.55
−0.57	0.06	10.53
5 023	5	0.10

V_{10}

Correlation matrix							Best fit		
	A_T	μ_T	σ_T	N_T	$1/\tau_T$	c_T	Value	Error	Err%
A_T	1.000	0.601	−0.997	0.001	−0.003	−0.003	7×10^3	5×10^3	71.43
μ_T	0.601	1.000	−0.592	−0.003	−0.005	0.003	17.40	0.002	0.01
σ_T	−0.997	−0.592	1.000	−0.001	0.000	0.000	0.049	0.008	16.33
N_T	0.001	0.003	−0.001	1.000	−0.949	0.430	7.2	0.1	1.39
$1/\tau_T$	−0.003	−0.005	0.000	−0.949	1.000	−0.596	−0.108	0.008	7.41
c_T	0.002	0.003	0.000	0.430	−0.596	1.000	3 288	4	0.12

N_{15}

Correlation matrix							Best fit		
	A_T	μ_T	σ_T	N_T	$1/\tau_T$	c_T	Value	Error	Err%
A_T	1.000	0.082	0.179	0.774	−0.783	0.559	1.01×10^3	0.08×10^3	7.92
μ_T	0.082	1.000	0.376	0.256	−0.252	0.155	17.24	0.06	0.35
σ_T	0.179	0.376	1.000	0.543	−0.549	0.382	1.06	0.05	4.72
N_T	0.774	0.256	0.543	1.000	−0.998	0.738	11.1	0.1	0.90
$1/\tau_T$	−0.783	−0.252	−0.549	−0.998	1.000	−0.750	−0.214	0.009	4.21
c_T	0.559	0.155	0.382	0.738	−0.750	1.000	11.14×10^3	0.01×10^3	0.09

N_{30}

Correlation matrix							Best fit		
	A_T	μ_T	σ_T	N_T	$1/\tau_T$	c_T	Value	Error	Err%
A_T	1.000	−0.139	0.176	0.693	−0.699	0.248	1.37×10^3	0.06×10^3	4.38
μ_T	−0.139	1.000	0.160	−0.039	0.047	−0.096	18.26	0.05	0.27
σ_T	0.176	0.160	1.000	0.604	−0.612	0.187	1.26	0.05	3.97
N_T	0.693	−0.039	0.604	1.000	−0.998	0.451	12.2	0.1	0.82
$1/\tau_T$	−0.699	0.047	−0.612	−0.998	1.000	−0.467	−0.30	0.01	3.33
c_T	0.248	−0.096	0.187	0.451	−0.467	1.000	11 206	9	0.08

N_{50}

Correlation matrix							Best fit		
	A_T	μ_T	σ_T	N_T	$1/\tau_T$	c_T	Value	Error	Err%
A_T	1.000	−0.997	−0.999	0.023	−0.025	0.013	0.1×10^6	0.9×10^6	900.00
μ_T	−0.977	1.000	0.970	−0.039	0.043	−0.021	17.81	0.02	0.11
σ_T	−0.999	0.970	1.000	−0.019	0.019	−0.011	0.03	0.03	100.00
N_T	0.023	−0.039	−0.019	1.000	−0.985	0.504	10.69	0.05	0.81
$1/\tau_T$	−0.025	0.043	0.019	−0.985	1.000	−0.576	−0.188	0.003	0.47
c_T	0.013	−0.021	−0.011	0.504	−0.576	1.000	11.08×10^3	0.01×10^3	0.09

Δ_{50}

Correlation matrix

	A_T	μ_T	σ_T	N_T	$1/\tau_T$	c_T
A_T	1.000	−0.101	0.159	0.685	−0.693	0.289
μ_T	−0.101	1.000	0.230	0.030	−0.022	−0.063
σ_T	0.159	0.230	1.000	0.585	−0.593	0.218
N_T	0.685	0.030	0.585	1.000	−0.998	0.510
$1/\tau_T$	−0.693	−0.022	−0.593	−0.998	1.000	−0.528
c_T	0.289	−0.063	0.218	0.510	−0.528	1.000

Best fit

Value	Error	Err%
1.34×10^3	0.06×10^3	4.48
18.16	0.05	0.28
1.19	0.05	4.20
12.08	0.1	0.83
−0.284	0.01	3.52
11.94×10^3	0.01×10^3	0.08

Δ_{30}

Correlation matrix

	A_T	μ_T	σ_T	N_T	$1/\tau_T$	c_T
A_T	1.000	−0.045	0.132	0.671	−0.682	0.298
μ_T	−0.045	1.000	0.321	0.125	−0.119	−0.002
σ_T	0.132	0.321	1.000	0.557	−0.566	0.224
N_T	0.671	0.124	0.557	1.000	−0.997	0.513
$1/\tau_T$	−0.682	−0.119	−0.566	−0.997	1.000	−0.532
c_T	0.298	−0.002	0.224	0.513	−0.532	1.000

Best fit

Value	Error	Err%
1.25×10^3	0.06×10^3	4.80
18.17	0.05	0.28
1.14	0.05	4.39
11.8	0.1	0.85
−0.260	0.008	3.08
11 881	9	0.08

Δ_{20}

Correlation matrix

	A_T	μ_T	σ_T	N_T	$1/\tau_T$	c_T
A_T	1.000	−0.211	−0.045	0.524	−0.524	0.071
μ_T	−0.211	1.000	0.026	−0.266	0.277	−0.257
σ_T	−0.045	−0.026	1.000	0.466	−0.468	−0.001
N_T	0.524	−0.266	0.466	1.000	−0.998	0.472
$1/\tau_T$	−0.524	0.227	−0.468	−0.998	1.000	−0.500
c_T	0.071	−0.257	−0.001	0.472	−0.500	1.000

Best fit

Value	Error	Err%
1.50×10^3	0.05×10^3	3.33
18.29	0.05	0.27
1.27	0.04	3.15
13.0	0.1	0.77
−0.36	0.01	2.78
11.17×10^3	0.02×10^3	0.18

Δ_{10}

Correlation matrix

	A_T	μ_T	σ_T	N_T	$1/\tau_T$	c_T
A_T	1.000	−0.055	0.146	0.680	−0.689	0.311
μ_T	−0.055	1.000	0.296	0.106	−0.099	−0.014
σ_T	0.146	0.296	1.000	0.567	−0.576	0.235
N_T	0.680	0.106	0.567	1.000	−0.998	0.530
$1/\tau_T$	−0.689	−0.099	−0.576	−0.998	1.000	−0.549
c_T	0.311	−0.014	0.235	0.530	−0.549	1.000

Best fit

Value	Error	Err%
1.27×10^3	0.06×10^3	4.72
18.17	0.05	0.28
1.15	0.05	4.35
11.8	0.1	0.85
−0.265	0.008	3.02
11 189	9	0.08

Bibliography

[1] C. Giunti and C. W. Kim, "Fundamentals of Neutrino Physics and Astrophysics", Oxford University Press, mar 2007.

[2] S. Weinberg, "A Model of Leptons", *Phys. Rev. Lett.* **19** nov (1967) 1264–1266.

[3] S. Chatrchyan, V. Khachatryan, A. M. Sirunyan, et al., "Observation of a new boson at a mass of 125 GeV with the CMS experiment at the LHC", *Physics Letters, Section B: Nuclear, Elementary Particle and High-Energy Physics* **716** (2012), no. 1, 30–61, 1207.7235.

[4] S. Chatrchyan, V. Khachatryan, A. M. Sirunyan, et al., "Measurement of the properties of a Higgs boson in the four-lepton final state", *Physical Review D - Particles, Fields, Gravitation and Cosmology* **89** (2014), no. 9, 1–45.

[5] T. Kajita and A. B. McDonald, "The Nobel Prize in Physics 2015", 2015. http://www.nobelprize.org

[6] A. D. Sakharov, "Violation of CP Invariance, c Asymmetry, and Baryon Asymmetry of the Universe", *Pisma Zh. Eksp. Teor. Fiz.* **5** (1967) 32–35.

[7] J. Beringer and Others, "Review of Particle Physics (RPP)", *Phys.Rev.* **D86** (2012), no. 9, 10001, arXiv:0601168.

[8] D. Gastler, E. Kearns, A. Hime, et al., "Measurement of scintillation efficiency for nuclear recoils in liquid argon", *Physical Review C* **85** jun (2012) 065811, 1004.0373.

[9] Y. Fukuda, T. Hayakawa, E. Ichihara, et al., "Evidence for Oscillation of Atmospheric Neutrinos", *Physical Review Letters* **81** (1998), no. 8, 1562–1567, arXiv:9807003.

[10] H. Ishino, "Gadolinium study for Super-Kamiokande", 2009.

[11] K. Lechner, "Elettrodinamica Classica", Springer, 2012.

[12] E. O. Wilhelmi, "Separación gamma/hadrón con el telescopio MAGIC", PhD thesis, Universidad Complutense de Madrid, 2001.

[13] K. Shiba, "Measurements of Neutron Thermalization Parameters in Light Water by Pulsed Source and Non 1/ v Absorber Method", *Journal of Nuclear Science and Technology* **5** (1968), no. 5, 201–209.

[14] M. Fujino and K. Sumita, "Measurements of neutron thermalization time constant of light water by pulsed neutron method", *Journal of Nuclear Science and Technology* **7** (1970), no. 6, 277–284.

[15] A. Renshaw, "Research and Development for a Gadolinium Doped Water Cherenkov Detector", *Physics Procedia* **37** (2012), no. 0, 1249–1256.

[16] G. Leinweber, D. Barry, M. Trbovich, et al., "Neutron capture and total cross-section measurements and resonance parameters of gadolinium", *Nucl. Sci. Eng.* **154** (2006) 261–279.

[17] S. Dazeley, A. Bernstein, N. Bowden, and R. Svoboda, "Observation of neutrons with a Gadolinium doped water Cherenkov detector", *Nuclear Instruments and Methods in Physics Research Section A: Accelerators, Spectrometers, Detectors and Associated Equipment* **607** aug (2009) 616–619, 0808.0219.

[18] I. Anghel, J. F. Beacom, M. Bergevin, et al., "Expression of Interest: The Atmospheric Neutrino Neutron Interaction Experiment (ANNIE)", 1402.6411.

[19] K. Hiraide, J. L. Alcaraz-Aunion, S. J. Brice, et al., "Search for charged current coherent pion production on carbon in a few-GeV neutrino beam", *Physical Review D* **78** dec (2008) 112004, 1011.2131.

[20] K. Abe, J. Adam, H. Aihara, et al., "Observation of electron neutrino appearance in a muon neutrino beam.", *Physical review letters* **112** feb (2014) 061802, 1311.4750.

[21] T. Katori, "Meson Exchange Current (MEC) Models in Neutrino Interaction Generators", 1304.6014.

[22] J. T. Sobczyk, "Multinucleon ejection model for Meson Exchange Current neutrino interactions", 1201.3673.

[23] J. Grange and T. Katori, "Charged current quasi-elastic cross-section measurements in MiniBooNE", *Modern Physics Letters A* **29** apr (2014) 1430011, 1404.6484.

[24] A. A. Aguilar-Arevalo, C. E. Anderson, A. O. Bazarko, et al., "First measurement of the muon neutrino charged current quasielastic double differential cross section", *Physical Review D - Particles, Fields, Gravitation and Cosmology* **81** (2010), no. 9, 1–22, 1002.2680.

[25] A. A. Aguilar-Arevalo, B. C. Brown, L. Bugel, et al., "First measurement of the muon antineutrino double-differential charged-current quasielastic cross section", *Physical Review D - Particles, Fields, Gravitation and Cosmology* **88** (2013), no. 3, 1301.7067.

[26] R. A. Smith and E. J. Moniz, "Neutrino Reactions on Nuclear Targets", *Nuclear Physics, Section B* **43** (1972), no. 2, 605–622.

[27] M. Martini, M. Ericson, G. Chanfray, and J. Marteau, "Neutrino and antineutrino quasielastic interactions with nuclei", *Physical Review C - Nuclear Physics* **81** (2010), no. 4, 1–5, 1002.4538.

[28] J. Nieves, I. Ruiz Simo, and M. J. Vicente Vacas, "The nucleon axial mass and the MiniBooNE quasielastic neutrino-nucleus scattering problem", *Physics Letters, Section B: Nuclear, Elementary Particle and High-Energy Physics* **707** (2012), no. 1, 72–75, 1106.5374.

[29] MiniBooNE Collaboration, "The Neutrino Flux prediction at MiniBooNE", *Physical Review D - Particles, Fields, Gravitation and Cosmology* **79** jun (2008) 1–38, 0806.1449.

[30] MiniBooNE Collaboration, SciBooNE Collaboration, G. Cheng, et al., "Dual baseline search for muon antineutrino disappearance at $0.1\ \text{eV}^2 < \Delta m^2 < 100\ \text{eV}^2$", *Physical Review D - Particles, Fields, Gravitation and Cosmology* **86** aug (2012) 1–15, 1208.0322.

[31] Y. Abe, C. Aberle, J. C. dos Anjos, et al., "First measurement of $\theta 13$ from delayed neutron capture on hydrogen in the Double Chooz experiment", *Physics Letters, Section B: Nuclear, Elementary Particle and High-Energy Physics* **723** (2013), no. 1-3, 66–70, 1301.2948.

[32] S. Dazeley, A. Bernstein, and N. Bowden, "The Watchboy Radionuclide Detector Deployment and Analysis", *LLNL-TR-661658*, 2014.

[33] N. Barros, T. Kaptanoglu, B. Kimmelman, et al., "Characterization of the ETEL D784UKFLB 11 inch Photomultiplier Tube", 1512.06916.

[34] S. M. George, "Atomic layer deposition: An overview", *Chemical Reviews* **110** (2010), no. 1, 111–131.

[35] Y. Nakajima, "A Measurement of Neutrino Charged Current Interactions and a Search for Muon Neutrino Disappearance with the Fermilab Booster Neutrino Beam", PhD thesis, Kyoto Univesity, 2011.

[36] J. Walding, G. P. Zeller, J. G. Morfin, and F. Cavanna, "The Muon Range Detector at SciBooNE", in "AIP Conference Proceedings", vol. 967, pp. 289–291. AIP, 2007.

[37] B. Richards, "ToolDAQ DAQ Framework", 2016. 7th Open Meeting for the Hyper-Kamiokande Project.

[38] J. Rynearson, "VME320 / 2eSST Protocol", 1998. http://www.vita.com/VME320-2eSST-Protocol.

[39] M. Tecchio, J. Ameel, M. Bogdan, et al., "The Data Acquisition System for the KOTO Detector", *Physics Procedia* **37** (2012) 1940–1947, arXiv:1406.3907.

[40] iMatix, "ZeroMQ", 2016. http://www.zeromq.org.

[41] S. Brice, R. Cooper, F. DeJongh, et al., "A method for measuring coherent elastic neutrino-nucleus scattering at a far off-axis high-energy neutrino beam target", *Physical Review D* **89** apr (2014) 072004, 1311.5958.

[42] B. Fellenz and J. Crisp, "An improved resistive wall monitor", 1998.

[43] P. Theodórsson, "Measurement of Weak Radioactivity", Word Scientific, 1996.